Self-assembly of Tyrosine-containing Peptides into Injectable Hydrogels with Distinct Nanostructures is Key in Determining Inflammatory Response of Macrophages

Jacek K. Wychowaniec,[1,*] Ezgi Irem Bektas,[1] Andrea J. Vernengo,[1,δ] Marcia Mürner[1,3], Marielle Airoldi,[1] Charlotte J.C. Edwards-Gayle,[2] Paul Sean Tipay,[4] Jiranuwat Sapudom,[5] Jeremy Teo,[5] David Eglin,[6] and Matteo D'Este[1]

[1] AO Research Institute Davos, Clavadelerstrasse 8, Davos, 7270, Switzerland

[2] Diamond Light Source, Harwell Science and Innovation Campus, Fermi Avenue, Didcot, OX110DE, United Kingdom

[3] ETH Zürich, Zürich, 8093, Switzerland

[4] Independent Scholar

[5] Laboratory for Immuno Bioengineering Research and Applications, Division of Engineering, New York University Abu Dhabi, Abu Dhabi, 129188, United Arab Emirates

[6] Mines Saint-Étienne, Univ Jean Monnet, INSERM, U1059 Sainbiose, Saint-Étienne, France

[δ] Current address: Henry M. Rowan College of Engineering, Department of Chemical Engineering and Biomedical Engineering, Rowan University, Glassboro, NJ, USA

*Corresponding author J.K.W.

e-mail: jacek.wychowaniec@aofoundation.org

Graphical Abstract

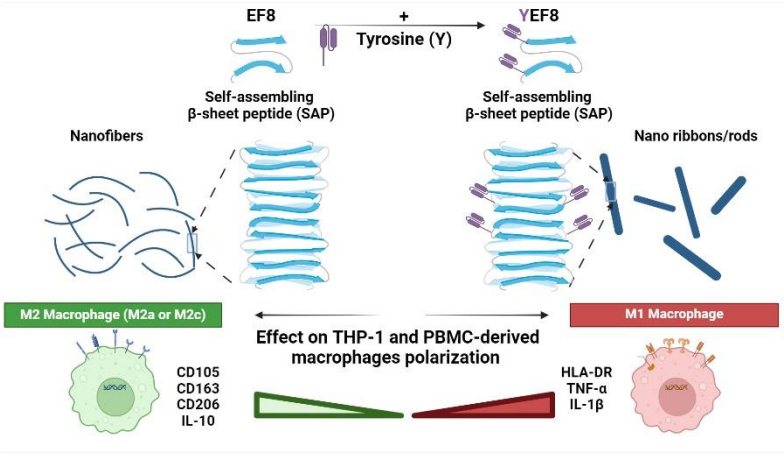

Keywords: Tyrosine-modified self-assembling peptides; Nanostructured peptides; Macrophage Polarization; Inflammation; Immunomodulation

Abstract

Self-assembling peptides (SAPs) are fully defined nanobiomaterials offering unprecedented opportunities to control nanostructure and chemical attributes to investigate and manipulate cellular signals. To investigate the influence of chemical and morphological characteristics on inflammatory signalling in native immunity, we designed five β-sheet SAPs: EFEFKFEFK (**EF8**), **Y**EFEFKFEFK (**YEF8**), **Y**EFEFKFEFK (**EF8Y**), **Y**EFEFKFEFK (**YEF8Y**) and E**Y**EFKFEFK (**EYF8**) (F: phenylalanine; E: glutamic acid; K: lysine, **Y**: tyrosine). The position of tyrosine in the peptide sequence dictated the distinct self-assembly into nanostructures, with sequences **EF8Y**, **YEF8Y**, **EYF8** self-assembling into thin nanofibers $d \approx 3.8 \pm 0.2$ nm, **YEF8** self-assembling into rod-like flat ribbons $d > 20$ nm and **EF8** (control) consisting of both types of self-assembled nanostructures. These distinct nanostructures induced contrasting inflammatory response of monocytic model THP-1 cells-derived macrophages (MΦs). Presence of soluble **EF8** nanofibers (at 2 mM) induced anti-inflammatory response and polarization towards an M2 state, whereas **YEF8** displayed tendency for inducing pro-inflammatory response and polarization towards M1 state. The **EF8Y**, **YEF8Y**, **EYF8** SAPs did not induce an inflammatory response in our models. These results were validated using peripheral blood mononuclear cells (PBMCs)-derived MΦs from human donors, confirming the critical role of the **EF8** and **YEF8** SAPs as possible orchestrators of the repair of tissues or inducers of pro-inflammatory state, respectively. These findings will facilitate the utilization of this family of SAPs as immunomodulatory nanobiomaterials potentially changing the course of inflammation during the progression of various diseases.

Introduction

Multifunctional biomaterials which exhibit well-defined physicochemical properties and encode spatiotemporally controlled biological signals are emerging as next generation advanced cell culture and organoids growth systems. In particular, producing and manipulating a complexity of custom instructive immunological cellular signals are key factors to achieve appropriate tissue regeneration.[1] This arises from the essential role played by both the innate and adaptive parts of immune system in inducing normal healing of damaged tissues, mediated by inflammation.[2] After injury, inflammation is the trigger of tissue repair, however chronic inflammation is detrimental. The fine balance between these two fates is context-dependent.[3,4] These effects are both associated with the phenotypic state of the immune cells present at the injury site, as well as the chosen treatment method, covering a vast array of cell types and signalling pathways. These include dendritic cells, monocytes, neutrophils, macrophages (MΦs), T-cells and B-cells, as well as cytokines, chemokines, growth factors, and molecular interactions between all components, overall creating a complex inter-linked system that orchestrates the progression and resolution of any healing process.[5] MΦs are involved in the inflammatory, proliferative and remodelling phases of wound healing,[6] and they produce a wide range of cytokines and chemokines that initiate subsequent clearance and drive tissue to natural homeostasis state.[7] MΦs exist on a spectrum of polarization that ranges from a pro-inflammatory M1 state, known as classically activated MΦs to a range of protective anti-inflammatory M2-like states, largely called alternatively-activated MΦs.[1,4,8] In general, M1 and M2 MΦs are two distinct phenotypes of macrophages with contrasting characteristics and functions. M1 MΦs are classically activated in response to pathogens, interferon-gamma (IFN-γ) and lipopolysaccharides (LPS) from bacteria, produce high levels of pro-inflammatory cytokines (IL-1β, IL-6, and TNF-α) and nitric oxide (NO), efficiently present antigens to T-helper 1 (Th1) cells, and overall promote inflammation and host defence. In a wound, M1 typically phagocytises dead tissue, cells and bacteria preparing it for the subsequent healing phases. On the other hand, the set of M2

MΦs (covering M2a, M2b, M2c and M2d) are activated in response to different anti-inflammatory signals (including IL-4, IL-13, IL-10, TGFβ, TLR agonists and glucocorticoids) and are involved in tissue remodelling, producing arginase-1, and promoting wound healing and immunosuppression, depending on the exact M2 sub-phenotype.[1, 9, 10] The relative ratio of MΦs phenotypes should dynamically change during the course of tissue damage and repair, with M1 state mostly present in early inflammatory phase of an acute injury and M2 appearing through resolution and repair phase. MΦs immune signalling pathways convert external stimuli into cytosolic events associated with downstream adaptors and effectors undergoing substantial conformational changes and spatial reorganization upon ligand engagement.[11] Upon implantation, biomaterials provide biochemical and physical cues to MΦs.[12] Recent *in vitro* and *in vivo* studies have shown that certain biomaterials have inherent immunomodulatory properties capable of reducing the damaging innate inflammatory response caused by MΦ infiltration.[13-15] This process was shown to be important in inducing enhanced bone formation by either promotion of vascular invasion and instructed earlier inflammation,[14] or prolonged shift towards M2 MΦ phenotype.[16] From the nanomaterials perspective, it has been shown that nanofibers (in a range 100-1000 nm) produced by electrospinning, typically made of thermoplastic, e.g. polycaprolactone (PCL) or its copolymers, possess capacity to influence MΦ phenotype.[17] These studies have shown prevalent influence of the nanofibers of rather large size (>100 nm), without decoupling of the exact effect of their chemical make-up, or exact shape. On the other hand, there is only a handful of examples showing the effects of the self-assembled nanofibers in the scale <100 nm on MΦ phenotype.[18]

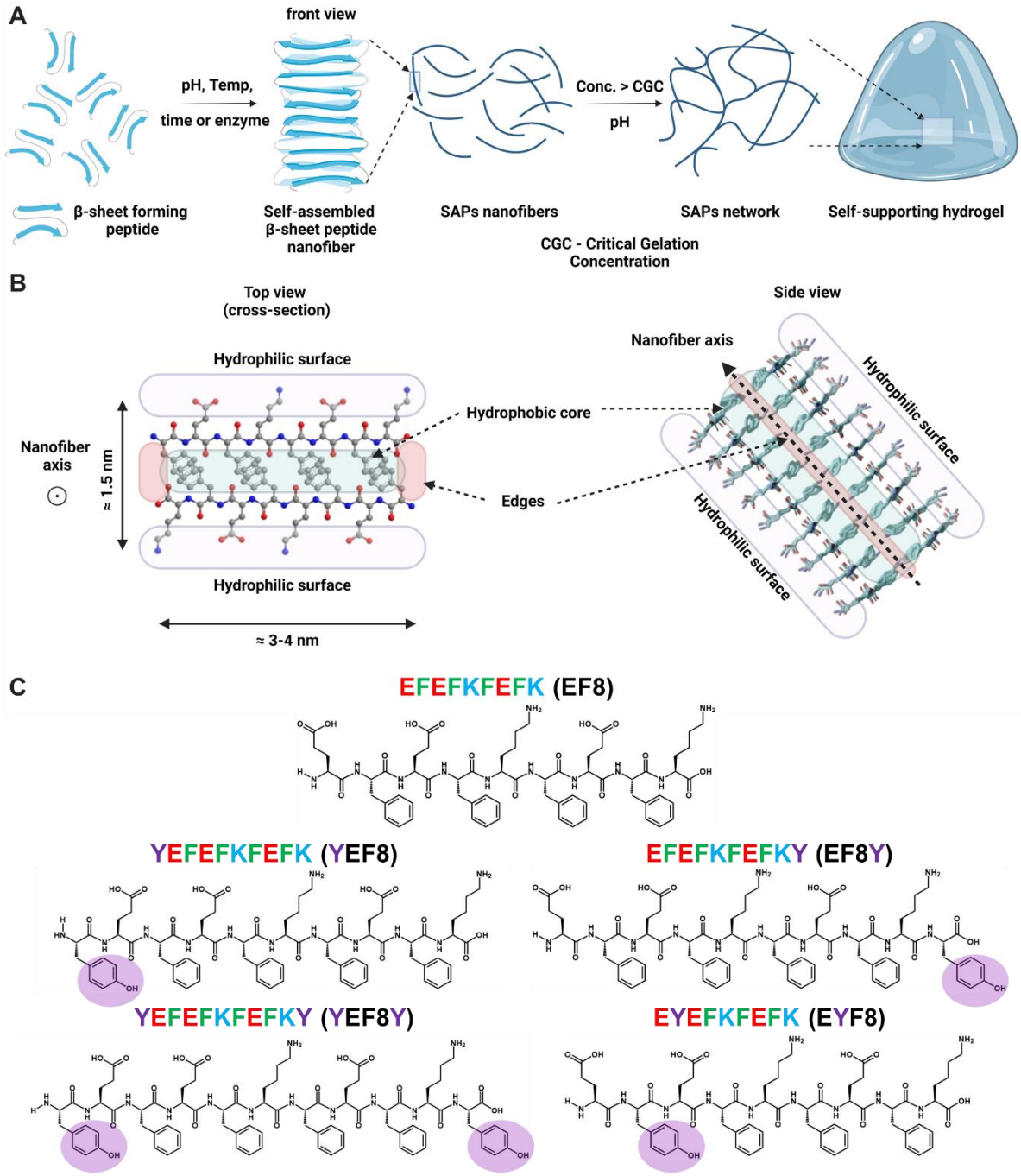

Figure 1. ***(A)*** *Schematic representation of the self-assembly and gelation pathway of β-sheet forming peptides. Created with BioRender.com.* ***(B)*** *Scheme of the formed nanofibers depicting top and side views. The peptide illustrated here is an original sequence FEFKFEFK (F8) (F: phenylalanine, E: glutamic acid, K: lysine), used for inclusion of tyrosine. The three shadings depict the relevant areas of nanofibers: hydrophilic surface, hydrophobic core, and edges.* ***(C)*** *Chemical structures of peptides used in this study. Sequence EF8 is a derivation of original F8 by inclusion of glutamic acid, whereas all further sequences are tyrosine-modified versions of EF8. Tyrosine is highlighted in purple.*

Molecular self-assembly is a natural phenomenon in which molecules spontaneously organise themselves into higher nanostructures, mainly via non-covalent interactions.[19] One of the most

biologically potent and interesting molecules are self-assembling peptides (SAPs), which as building blocks can be synthesized with high fidelity and high purity at reasonable costs, avoiding the batch-to-batch variation.[20] Due to their natural amino acid composition, peptides can be designed as either promoters or inhibitors of specific cellular processes.[21] Minimalistic approaches can also be used to find short peptide sequences with tendency for aggregation towards particular nanostructures.[22, 23] In fact, a variety of peptide designs can be found in the literature that self-assemble into fibers and above a critical gelation concentration (CGC) form hydrogels.[23, 24, 25, 26] Indeed, by the choice of primary peptide sequence, functional materials with defined nanostructure and responsiveness can be designed.[25, 26] So-called β-sheet SAPs are a class of attractive molecules for the design of biomaterials, in particular hydrogels, and emulgels/emulsions.[27, 28] These materials are highly hydrated and built from amphiphilic nanofibers that can mimic extracellular matrix (ECM),[29] and have been shown to be biocompatible and tailorable in terms of their physicochemical and biological properties. This includes the possibilities of their use in additive manufacturing,[30, 31] as well as translational potential as platforms for multiple organoids and cellular spheroids growth.[32, 33] Zhang's group devised one of the most popular and successful short SAPs designs: (**ABACABAC**)$_n$, based on the alternation of hydrophobic (**A**) and hydrophilic (**B**/**C**) amino acids, typically in the 4−20 total amino acids make up.[34] These often self-assemble into nanofibers in the diameter range of 2-10 nm, and above CGC form self-supporting hydrogels (***Figure 1A***). The key feature of this family of the antiparallel β-sheet peptide designs include formation of the nanofibers, where all the hydrophilic residue side groups face outer part and aqueous phase, whereas all the hydrophobic residue groups conceal and form a core (***Figure 1B***).[28] The typical characteristics of these nanofibers is their rectangular cross-section with a width ranging from 3 to 10 nm, depending on the length of the peptide used and a thickness of ~1.5 nm.[28] Noteworthy, these elemental nanofibers can laterally stack expanding in the overall diameter forming nanostructures up to 200 nm, depending on the exact amino acid composition and pH-driven electrostatic interactions.[26, 35, 36] The three key nanofiber structural (***Figure 1B***)

characteristics include: (i) hydrophilic surface which controls the nanofiber solubility and associative interactions with other nanofibers; (ii) hydrophobic core which controls the nanofiber morphology and shape, and (iii) edges, which can be both hydrophobic or hydrophilic and overall control interactions with other nanofibers and external molecules, e.g. drugs.[28, 37, 38] Chemical modifications of amino acid sequence, including edge-modifications and substitions, offer ways to influence the formation and size of the resulting nanostructure and the resulting bulk hydrogels' properties.[27, 28, 30, 38] This resulted in a large pool of the modifications of SAPs as potential immunomodulatory biomaterials. In particular, the group of Collier has shown that this class of SAP: i) can act as modulator of adaptive immunity, ii) can act as adjuvant and vaccines, and iii) can very well modulate antibody responses.[39] They also demonstated that a peptide FKFEFKFE (KFE8) is non-immunogenic to adaptive immunity.[40] Finally, they pointed out that the SAP negative surface charge prevented T-cell and antibody responses to antigen-carrying assemblies, whereas positive surface charge augmented the uptake of fibrillized peptides by antigen presenting cells, providing a benchmark of design to SAP peptide nanofibers.[41] On the other hand, Kumar *et al.* reported a similar SAP from this class, forming anti-parallel β-sheets, having no immunogenecity on the THP-1 derived MΦs.[18] The MΦs modulation was only shown when Monocyte Chemoattractant Protein-1 (MCP-1) and IL-4 were co-delivered from this SAP hydrogel, indicating its potential as a non-immunogenic delivery platform. Given that in general this class of SAP nanofibers in the 4-10 nm diameter range has been shown not to induce immunogenic responses, we were interested in demonstrating the possibility to modulate the native immunity based on the chemical or nanostructure aspects. Tyrosine is a versatile amino acid, both used for assembling functional materials,[42] as well as enabling subsequent chemical crosslinking and thus modulation of viscoelastic properties and stability of the formed materials.[43] Recently we have shown the effects of tyramine-modified hyaluronic acid (THA) hydrogels along various other biomaterials, on neutrophils, indicating relative lack of enhanced pro-inflammatory response compared to other studied materials.[13] We have also shown that low molecular weight of

soluble THA is mildly pro-inflammatory compares to high molecular weight in response to MΦs on PBMCs-derived MΦs.[44] Hence, in the current work, we chose to investigate the decoupling of the effects the chemical peptide make-up and the type of nanostructure formed on the MΦs, based on the selection of tyrosine-modified SAPs. For that purpose, we designed five β-sheet forming SAPs: EFEFKFEFK (**EF8**), **Y**EFEFKFEFK (**YEF8**), **Y**EFEFKFEFK (**EF8Y**), **Y**EFEFKFEFK (**YEF8Y**) and E**Y**EFKFEFK (**EYF8**) (F: phenylalanine; E: glutamic acid; K: lysine, **Y**: tyrosine). The chemical structures of all peptides are presented in ***Figure 1C***. The first sequence, **EF8**, is one amino acid add-on modification of the original FEFKFEFK (**F8**) peptide,[28, 45] resulting in nanofibers that are soluble and in principle carrying an overall charge of Z≈-1 at physiological pH.[46] The **EF8** sequence was placed as a control for this study due to its known capability of self-assembly into thin nanofibers.[46] Subsequently, tyrosine was included on the edges of the **EF8** peptide, either on the N-terminus (**YEF8**), C-terminus (**EF8Y**), or both N- and C- terminal parts (**YEF8Y**). Finally, the 2nd position phenylalanine in the control **EF8** was replaced by tyrosine to enable its closer spatial location and incorporation into the core of the nanofiber (**EYF8**). This overall generated a selection of new tyrosine-containing SAPs family. Self-assembly and gelation of all sequences were evaluated using titrations, oscillatory and rotational rheology, Fourier transform infrared spectroscopy (FTIR), transmission electron microscopy (TEM) and small angle X-ray scattering (SAXS). We stipulate that designing functional peptide-based nanobiomaterials that incorporate immunomodulatory effects, biocompatibility and that allow stable long-term polarization of MΦs is of high interest in tissue engineering and biofabrication communities,[12] and hence in the current work we evaluated the polarization effects of the SAPs, firstly with the monocytic model THP-1 cells-derived MΦs and subsequently with peripheral blood mononuclear cells (PBMCs)-derived MΦs. Genetically similar monocytic THP-1 cells enabled rapid screening of the immunomodulatory potential, whereas (PBMCs)-derived MΦs enabled validation towards clinical applications. M1/M2-like polarization modulation was unravelled by immunocytochemistry, flow cytometry, gene expression analysis and

ELISA assays. Finally, we attempted to correlate the distinct nanostructural features to the overall inflammatory profile and to provide a basis for rules governing the immunomodulatory tissue engineering of this family of SAP nanobiomaterials.

Results and Discussion

1. Self-assembly and gelation properties

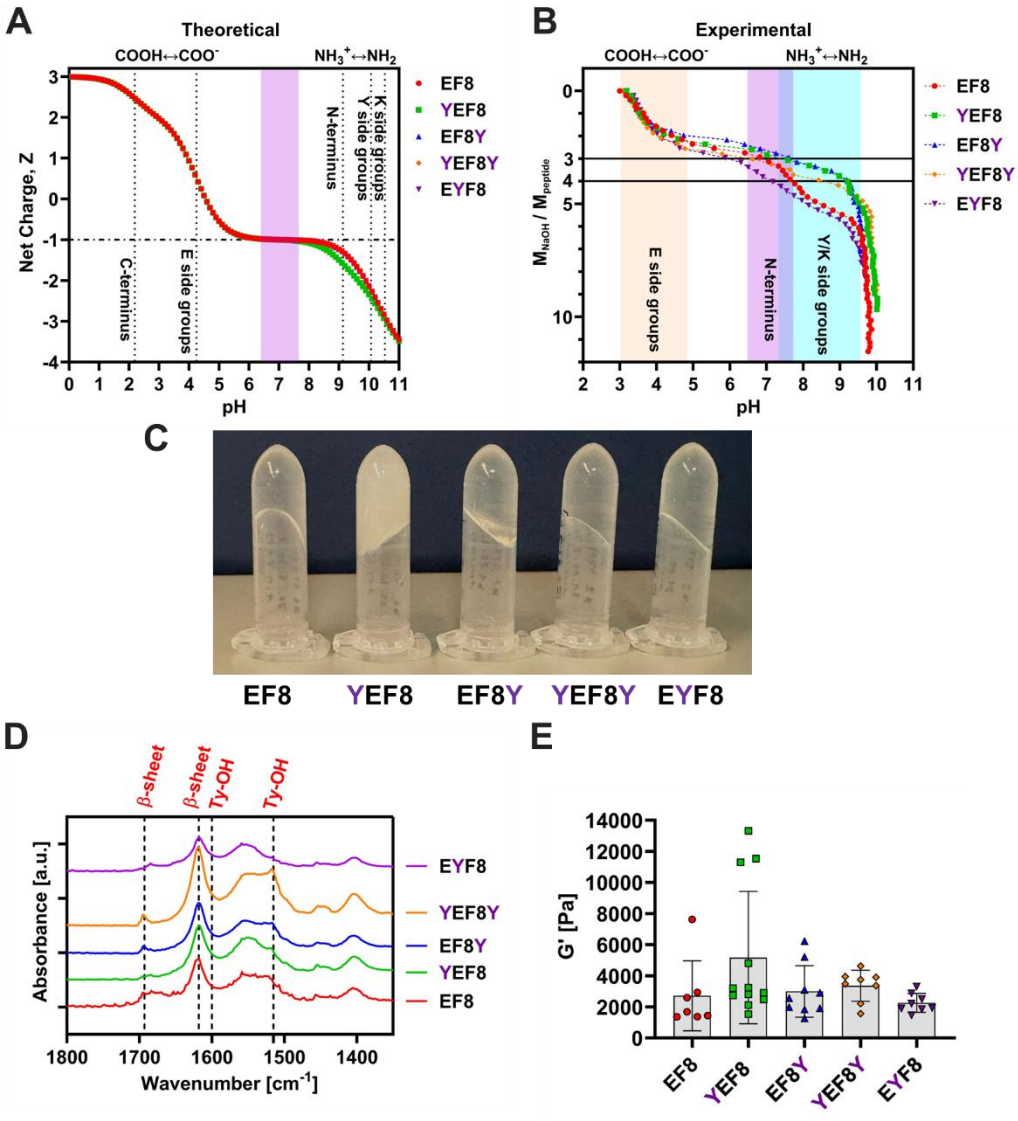

Figure 2. (A) *Theoretical charge carried by each peptide as a function of pH. Vertical dotted lines indicate the theoretical pK_a of the different ionic groups present on the peptides. Shaded region depicts physiological conditions. Horizontal dotted line depicts a charge state at physiological conditions of Z=-1 e^-.* ***(B)*** *Molar ratio of added NaOH to peptide as a function of pH. Shadowed regions indicate the protonation/deprotonation transition regions of the different ionic groups (E: Glutamic acid, K: Lysine, Y: Tyrosine). Horizontal lines depict region of 3 – 4 equivalents of deprotonation of moles of peptide. Theoretically 3 molar equivalents of NaOH are required to*

deprotonate all glutamic acids presents on each peptide. ***(C)*** *Photograph of SAP hydrogels prepared at 20 mM and at physiological pH.* ***(D)*** *ATR-FTIR spectra obtained for all hydrogels prepared at a concentration of 20 mM. Vertical dashed lines indicate the position of the two bands characteristic of adoption by peptides of β-sheet conformations as well as tyrosine specific peaks.* ***(E)*** *Storage modulus (G') for different designed peptide hydrogels at 20 mM concentration taken at ~0.162% strain and 1 Hz frequency from multiple amplitude sweeps and at 0.2 % strain and 1 Hz from frequency sweeps. In total 5-6 repeats of independently prepared hydrogels are shown. Amplitude sweeps are provided in Supporting Information (****Figure S2****).*

The charge of SAPs has been shown to affect the immunogenicity and interactions with immune cells,[41] hence our first aim was to evaluate it for all of our chosen SAPs at physiological pH. All peptides self-assembled into hydrogels above CGC of ≈ 2.5 mM (***Figure S1***). Hydrophilic amino acids present on the peptides (***Figure 1C***) contain ionic groups that can be deprotonated, in particular here: carboxylic acid ($COOH \leftrightarrow COO^-$) at the C-terminus (theoretical $pK_a \approx 2.18$) and on the glutamic acid side chains (theoretical $pK_a \approx 4.25$) and amine ($NH_3^+ \leftrightarrow NH_2$) at the N-terminus (theoretical $pK_a \approx 9.13$ and ≈ 8.95 on F and K side, respectively) and on the lysine side chains (theoretical $pK_a \approx 10.53$),[47] as well as ($OH \leftrightarrow O^-$) side group on tyrosine (theoretical $pK_a \approx 10.07$), that is prone for formation of additional hydrogen bonding.[47, 48] Previously, it was shown that titrations can shift apparent pK_a values of the amino acids due to the occurrence of self-assembly and chemical environment,[28, 49] which was demonstrated by a large spread for calculated pK_a values of individual side chains in folded proteins.[50] As a result, the pH and thus electrostatic interactions, were shown to play a key role in the self-assembly and gelation properties of this family of β-sheet forming peptides.[28, 49, 51] In ***Figure 2A***, the theoretical charge carried by all the peptides as a function of pH is depicted, along with highlighted pK_a values of the different ionic groups. As can be seen, given that all peptides contain the same number of glutamic acids (3) and lysine (2) residues, theoretically all peptides should behave almost the same, except for minor deviation of **YEF8** peptide in the pH region 8-10 (***Figure 2A***). Given that deprotonated tyrosine group is predominantly forming hydrogen bonds, theoretically, all peptides should carry a charge of $Z \approx -1$ at physiological pH. However, the difference in experimental pK_a values is expected due to the

changes in the local chemical environment in which the ionic groups reside.[49, 52] To investigate the exact effect of the self-assembly on the pK_a of the different ionic groups, all peptides were titrated in a solution state at a concentration of 1 mM (***Figure 2B***). This concentration is typically 1000 larger than the minimum fibrillization concentration of this class of SAPs.[53] The peptides used for this study were purchased as HCl salts, and as a result, when solubilized in water, the pH of all the solutions was acidic, at value of 3.1 ± 0.2. These pH values are above the theoretical pK_a value of the C-terminus COOH end groups. It can therefore be assumed that these groups are deprotonated prior to titration experiments, whereas all other ionic groups remain protonated.[28] Immediately upon addition of the NaOH, a pK_a-like transition is observed between pH 3.0 and 4.8 for all peptides, indicating the deprotonation of the carboxylic acid groups on the glutamic acid side chains. Due to presence of 3 glutamic acids in each peptide, it is expected that this transition is complete when 3 moles of NaOH are added for each mole of peptide present. By inspection of the titration curve, the two glutamic acids are deprotonated faster, likely the first two in each peptide sequences starting from N-terminus, due to lower electrostatic attraction to the neighbouring positive charges. The final glutamic acid placed in the vicinity of the two lysine residues for each peptide sequence is held by stronger electrostatics forces and hence its full deprotonation requires a larger amount of base. As a result, the final glutamic acid deprotonation is achieved at pH 6.9 ± 0.2 for **EF8**; pH 7.3 ± 0.1 for **YEF8** and **EF8Y**; and pH 6.1 ± 0.3 for **EYF8** and **YEF8Y**. The pH at which this transition is observed suggests a shift of about 1 pH unit toward lower values for the pK_a of the carboxylic acid side groups in all sequences. This shift is larger than for the paternal **F8** sequence observed in the past, stemming from the additional glutamic acid closest to the N-terminus side of each peptide.[28] Previously, it has been shown that the transition from cloudy to clear hydrogels in these SAPs correlates with the increase in inter-peptide electrostatic repulsion, when modulus of charge $|Z| > 1$.[28, 36, 54] All SAPs also form self-supporting clear hydrogels (above similar CGC ~2.5 mM) except for **YEF8**, which retains cloudiness at this pH and at 20 mM concentration (***Figure 2C***). Considering that fact and the detailed aspects of

the subsequent deprotonation of the NH_3^+ side chains (see supporting information paragraph), in summary, titrations revealed that all SAPs carry a charge in the range $-2 \leq Z \leq -1$ at physiological pH (7.2 ± 0.2). By fixing charge across all SAPs, any subsequent immunological effects observed between different SAPs should not be due to the charge effects. Hence, from here on, all peptide solutions or hydrogels were prepared at that pH range.

The formation of β-sheet conformation was confirmed using ATR-FTIR (***Figure 2D***). All peptides were characterized by strong transmittance bands at 1618 cm^{-1} and bands in the region of 1684-1693 cm^{-1}, characteristic of the adoption by the peptides of β-sheet conformations.[20, 55, 56] The observed differences in the 1684-1694 cm^{-1} region are indicative of the minor changes in the structural packing of the sheets. Two main differences between peptides were observed. First, **EF8Y** clearly had stronger band at 1694 cm^{-1} compared to co-existence of two bands, 1984 and 1695 cm^{-1}, for **YEF8** (***Figure 2D***). Second, the β-sheet band has clearly shifted to a lower value of 1684 cm^{-1} for **EYF8**. Barth speculated that the high-wavenumber side band in the 1684-1694 cm^{-1} is often, but not always, absent for parallel β-sheets and that this band depends on the exact number of strands.[55] This indicates minor changes to the conformational adaptation of β-sheets for these peptides. Next, we observed differences in the amide II region (1500−1580 cm^{-1}, ***Figure 2D***). To analyse this region, we assumed that all peptides have a similar propensity to form β-sheets at the selected pH and hence normalized the spectra to the main β-sheet band at 1618 cm^{-1} (***Figure S2***). Given that there exist two tyrosine side chain specific bands,[57] one prominent at 1517 cm^{-1} and another one known to occur at the 1600 cm^{-1} shoulder (***Figure 2D***), we calculated their ratio for all peptides. This ratio could be indicative of the degree of exposure of tyrosine outside of the nanofiber. The following values were obtained: $I_{1517/1600}$=1.33, $I_{1517/1600}$=1.17, $I_{1517/1600}$=1.49, $I_{1517/1600}$=1.75, and $I_{1517/1600}$=0.81 for **EF8**, **YEF8**, **EF8Y**, **YEF8Y** and **EYF8**, respectively. Whilst **EF8** does not contain tyrosine, the tyrosine side chain groups are more exposed going from **YEF8** to **EF8Y** and **YEF8Y**, as observed by the increased ratio $I_{1517/1600}$ (***Figure S2***). Much lower ratio for **EYF8** indeed indicates the tyrosine side

chain is buried inside the aromatic core of the nanofiber (***Figure 1B-C***). Overall, data are indicative that all peptides follow to a varying extent similar anti-parallel β-sheet conformation at physiological pH.[55]

Viscoelastic features of soft materials have been shown to be a key cell-instructing factor,[58, 59] and we have also previously shown influence of variable stiffness of peptide hydrogels in the development of organoids.[32] Therefore, for all bulk hydrogels, prepared at 20 mM concentration, we run amplitude (***Figure S3***) and frequency (***Figure S4***) sweeps. We found that storage modulus (G′) was typically an order of magnitude larger than loss modulus (G″) in the linear viscoelastic region (LVR, ***Figure S3***) and in the linear frequency region (***Figure S4***, $0.1 < f < 10$ Hz), confirming the soft solid-like nature of these hydrogels. By taking storage modulus from multiple runs at values $\varepsilon \approx 0.2$ % and $f \approx 1$ Hz, we compared the storage modulus across all formulations and concluded that there were no statistical differences between any of them (***Figure 2E***). We noticed that peptide **YEF8** had largest spread of storage modulus, correlating well to the observed cloudy-like bulk hydrogel state. The storage modulus of all SAPs fall in the range of 3.4 ± 2.8 kPa, broadly covering a range of acceptable biomechanical values for soft tissues,[58] indicating that any observed effects in cellular behaviour between these sequences should not directly be linked to any difference in stiffness, as will be discussed in later section.

2. Structural assessment of SAPs by TEM and SAXS.

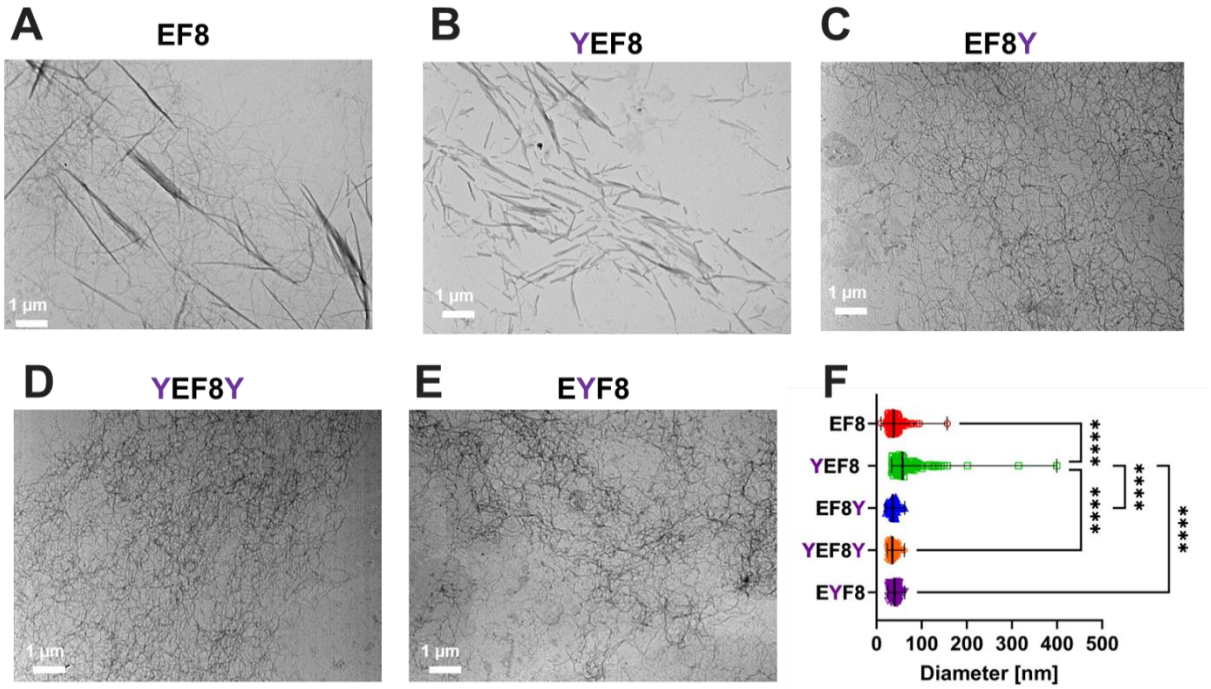

Figure 3. *TEM images obtained for:* ***(A) EF8****,* ***(B) YEF8****,* ***(C) EF8Y****,* ***(D) YEF8Y****,* ***(E) EYF8*** *diluted hydrogels prepared originally at 20 mM concentration.* ***(F)*** *measured fiber and fiber bundle width measurements. Each point defines 1 measurement across nanofiber or nanofiber bundle width. Median with range is plotted for each peptide. A statistically significant results were considered for p<0.05 (* - <0.05, ** - <0.01, *** - <0.005 and **** - <0.001).*

Nanofiber sizes and morphologies were characterized using transmission electron microscopy (TEM, ***Figure 3***) and small-angle X-ray scattering (SAXS, ***Figure 4***). TEM revealed obvious β-sheet rich entangled nanofibers and networks in all SAP hydrogels. **EF8** consisted of the thinnest nanofibers population with diameter in the range of 10 nm, and some small population of larger rod-like objects (***Figure 3A***). Our previous work demonstrated that thinnest nanofibers for **EF8** form in the range 1.51 ± 0.43 nm,[46] however we note this measurement was carried out on samples prepared directly in a solution form at 0.5 mM, rather than measured on diluted bulk hydrogels like here. This sample preparation leads to observations of much thicker stacks of fibrillar bundles rather than individual smallest nanofibers. This reflects typically denser 3D environment of a bulk hydrogel.

YEF8 distinctly consisted of larger rod and ribbon-like nanostructured objects (***Figure 3B***), whereas **EF8Y**, **YEF8Y** and **EYF8** all formed well-defined thin-fibrillar networks (***Figure 3C-E***).

The types of formed nanostructures are consistent with the formation of β-sheet-rich nanofibers and confirm the minor variations in the type of nanostructures formed observed by FTIR. The average widths ± SD obtained from TEM are 41 ± 15, 73 ± 50, 37 ± 8, 36 ± 7, and 40 ± 8 nm for **EF8**, **YEF8**, **EF8Y**, **YEF8Y** and **EYF8**, respectively. This indicates that the only sample statistically different sample compared to all other SAPs is **YEF8** ($p<0.001$), ***Figure 3F***. This confirms a more pronounced tendency for **YEF8** peptide to form aggregated β-sheet ribbon-like assemblies via lateral peptide stacking, compared to traditional bundling of β-sheet thin nanofibers observed for all other SAPs. TEM suggests that the control sequence, **EF8**, has small tendency for this formation, although β-sheet thin nanofibers remain a prevalent self-assembled nanostructure, as previously observed.[46] This also correlates well with the charge status of $-2 < Z < -1$ established in titrations (supporting information), indicating that a small fraction of objects may have lower charge (towards -1), leading to this observed aggregation and co-existence of predominant and expected nanofibrillar network and small fraction of ribbon-like assemblies.

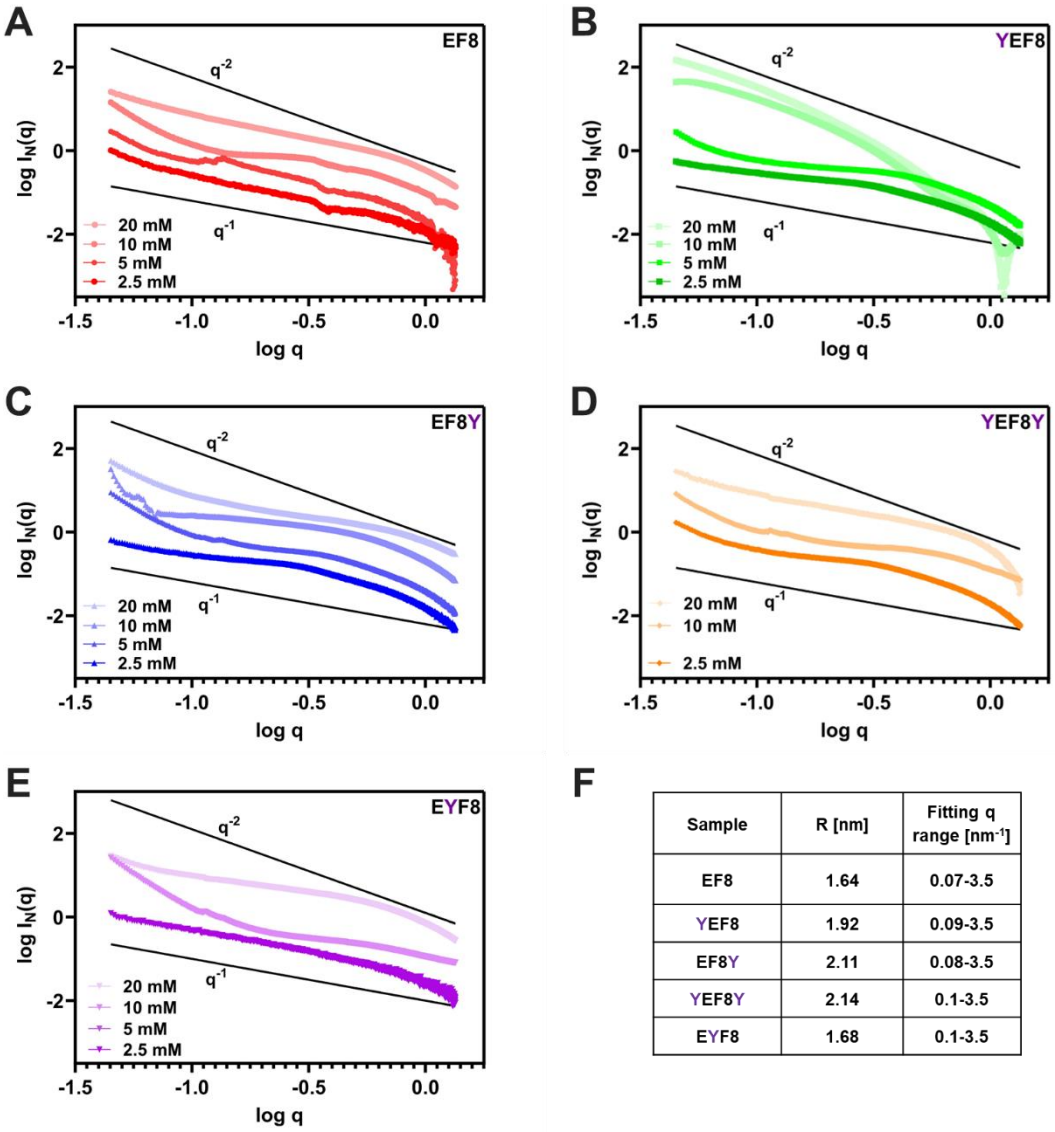

F

Sample	R [nm]	Fitting q range [nm^{-1}]
EF8	1.64	0.07-3.5
YEF8	1.92	0.09-3.5
EF8Y	2.11	0.08-3.5
YEF8Y	2.14	0.1-3.5
EYF8	1.68	0.1-3.5

Figure 4. *SAXS characterization of* ***(A) EF8****,* ***(B) YEF8****,* ***(C) EF8Y****,* ***(D) YEF8Y****,* ***(E) EYF8*** *hydrogels prepared at different concentrations (2.5, 5, 10 and 20 mM) in double logarithmic plot of $I_N(q)$ vs q representation. The straight lines depict type of slope for easier visualization. The reasons for missing 5 mM concentrations in plot D and E are explained in methods section.* ***(F)*** *Cylindrical fits to SAXS data of SAPs at 2.5 mM concentrations, where R is the fitted radius.*

We performed a structural analysis utilizing SAXS to confirm the presence of nanofibers and their dimensions for all SAPs. ***Figure 4*** shows the SAXS patterns obtained for all SAPs at various concentrations in the range 2.5 – 20 mM, presented as double logarithmic plots. For all samples prepared at 2.5 mM (on the border of CGC), a region of q^{-1} behaviour, typical of the scattering of rod-like objects, can be observed. For **EF8** and **EYF8** the q^{-1} region extends for most of the q-range (***Figure 4A*** and ***4E***). For all other SAPs, even at 2.5 mM, non-linear curves were observed, with

higher q regions following q^{-2} behaviour, often associated with flat ribbons, lamella, or disc-shaped particles.[30, 60] This indicates formation of flattened structures in the order of 5 – 20 nm, in line with our TEM observations. The size of these ribbons shifts as the concentration increases for **YEF8** sample towards low q region (***Figure 4B***), indicative of the formation of larger rod-like and ribbon-like bundles, again matching well with the observed nanostructures in TEM. Furthermore, this indicates that the critical transition and associative bundling for **YEF8** occurs above 5 mM concentration. For **EF8Y** and **YEF8Y** SAPs, the q^{-2} region persists in the order of 5 – 20 nm (higher q), confirming the structural built-up from individual nanofibers persists. The obtained shape of scattering also indicates that topologically the obtained networks vary from those previously published in the field, with more associative and heterogenous network of associated nanofibers, promoted by the introduction of edge-driven interactions.[28, 45] To confirm the individual built-up of all SAPs, we attempted fitting a cylindrical model (see methods) to the obtained curves at 2.5 mM concentrations (***Figure 4F***). In all cases, omitting small aggregation regions at low q values, we obtained good fits of individual infinite-like cylinders with radius in the range 1.9 ± 0.2 nm (diameters in the range of 3.8 ± 0.2 nm), in good agreement with the estimations for the nanofibers formed from this family of β-sheet SAPs.[28, 46]

All SAPs self-assembled into hydrogels above critical gelation concentration CGC≈2.5 mM, displayed characteristic high β-sheet content, similar built up from individual nanofibers with d≈3.8 ± 0.2 nm and larger associative flattened bundles in the range 5-20 nm, similar storage modulus, except for the **YEF8**, which retained cloudiness at physiological pH, had largest spread in storage modulus and was built up from much larger flattened ribbons/rods above 20 nm size. Altogether, the results from sections 1-2 indicate that the addition of the tyrosine residues does not affect the overall ability of the peptides to form β-sheet nanofibers, however it does affect the ability of these nanofibers to aggregate/associate and form larger fiber bundles, depending on the tyrosine position in the peptide sequence.

3. Rheological properties and embedded 3D printing of the SAP inks.

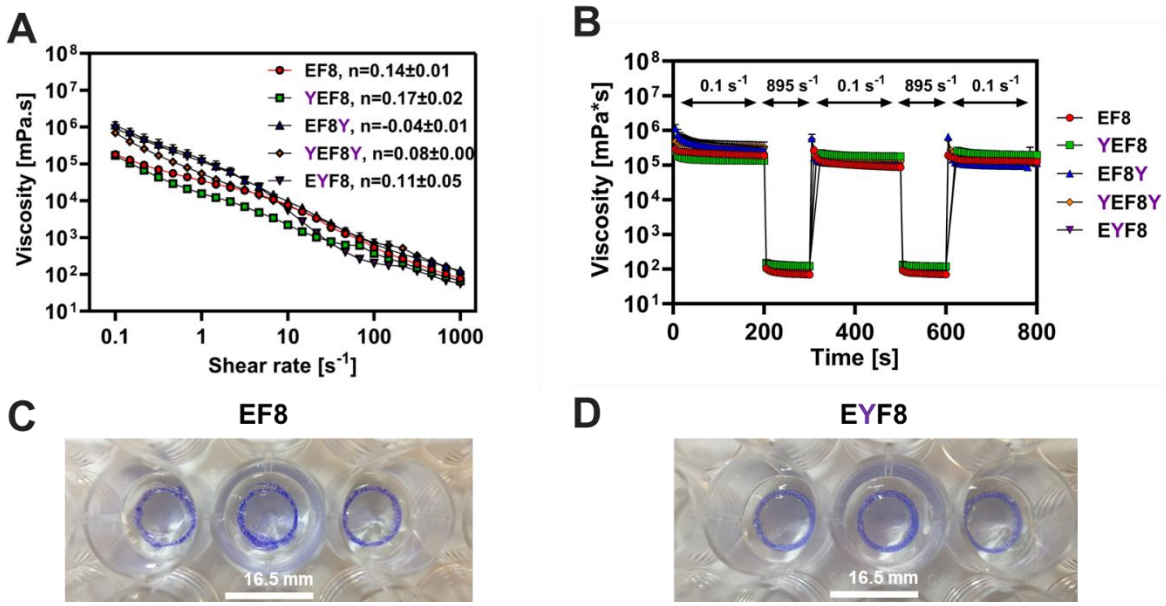

Figure 5. ***(A)*** *Steady flow experiments at 37 °C of all SAP hydrogels prepared at 20 mM concentration. Flow index (n) calculated using equation 2 (see methods) is provided for each peptide after its name. Error bars (SD) are included for all samples (n=2), however they might not be visible due to their small size.* ***(B)*** *Rotational flow recovery experiments at 37 °C of all SAP hydrogels prepared at 20 mM concentration. Average of n=2 is plotted, without error bars, as they would obscure the visibility of data. The used shear rate is plotted above each corresponding region. Digital photos of concentric circles printed into 3 neighbouring wells with 20 mM SAPs ink of* ***(C) EF8*** *and* ***(D) EYF8*** *into Carbopol bath.*

One key property of the developed SAP hydrogels is their injectability for minimally invasive surgery, and use in biomedical additive manufacturing.[61, 62] Therefore, we have measured viscosity curves and rotational flow recovery for all SAP hydrogels (hence named SAP inks) at 20 mM concentration. ***Figure 5A*** shows the viscosity curves at 37 °C which were fitted to a power law model (equation 2, Methods) to give shear-thinning exponents (*n*). All of SAPs followed n<1, indicating good downstream processability.[61] Flow recovery showed an immediate decrease of viscosity of about 3 orders of magnitude upon increase of shear rate, indicative of a transition to a low viscosity state (***Figure 5B***). This profile is indicative of increased extrudability or printability under the shear conditions present in the needle or nozzle. Upon cessation of the high shear conditions, representative of the material leaving the nozzle, the viscosity recovers to the same order of magnitude of the initial values, which is indicative of shape retention after extrusion. **YEF8** was the only SAP inks recovering

more than 100% of its initial viscosity 40 s after cessation of the high shear (***Figure 5B***, green squares). The peptide exhibited distinct behaviour compared to all other peptides, as evidenced by observations in TEM and its cloudiness in the gel form. This difference could be putatively attributed to the different nanostructure and network topology of **YEF8** compared to all other SAPs. The viscoelastic recovery of the tyrosine-containing SAP inks at the same 20 mM concentration was investigated also in oscillatory rheology, by applying low (0.2%) in alternation with high shear strain (100%) over 10 min intervals at a fixed frequency of 1 Hz (***Figure S5A***). **YEF8**, **EF8Y** and **YEF8Y** behaved similarly to the previous case of **F8** peptide,[28] with rather rapid and steady return to the original values, indicative of the types of networks with edge-driven adhesive points between nanofibers. In this test, **EYF8** SAP ink did not recover after the first interval, which might be indicative of different network morphology or of much longer relaxation processes in the network. The differences detected between oscillatory and flow recovery suggest also varying susceptibility of these types of materials to the type of applied shear.

Finally, to demonstrate simple printability of our formulations, we selected the control SAP **EF8**, and one tyrosine containing SAP, **EYF8** and demonstrated their freeform 3D printing. In ***Figure 5C-D*** inks were centrifuged at 1000 rcf for 5 minutes before printing, whereas in ***Figure S5B-C***, were centrifuged at 3220 rcf for 5 minutes before printing. We noticed that in the case of longer centrifuging time, qualitatively assessed thinner rings were obtained for **EYF8** on the expense of higher variation and inconsistencies of the structure. Hence, final structures could be modulated by the pre-conditioning step of the SAP ink in the cartridge (***Figure 5C-D*** and ***Figure S5B-C***). We chose Carbopol-based microgel bath and ring-like circular line structures as a simple model demonstrating that injectability and printing are possible, with obtained good structural fidelity. Multiple dynamic factors impact printing outcome, including barrel and needle temperature, extrusion pressure and head velocity.[61, 62] Bioink physicochemical parameters can also influence printability with changes to the rheological properties for example varying peptide concentration or compositing.[31, 62, 63]

4. Immunological effects exerted on genetically similar monocytic THP-1 cells-derived MΦs.

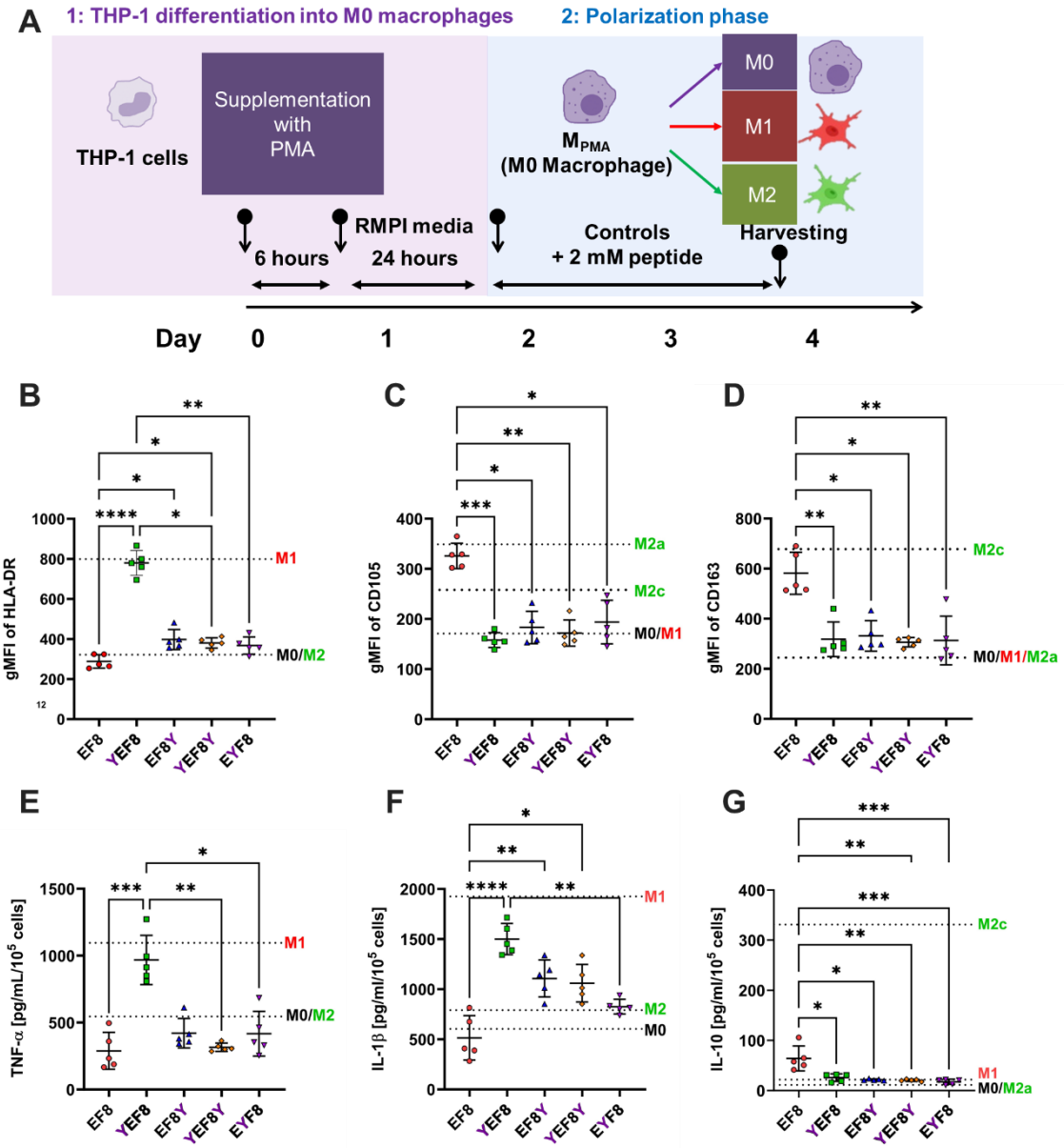

Figure 6. (A) *Scheme summarizing the differentiation protocol of THP-1-derived MΦs. THP-1 cells were differentiated into M0 MΦs by treatment with 300 nM phorbol-12-myristate-13-acetate (PMA) for 6 hours, followed by resting for 24 hours in cell culture media. Subsequently, M0 MΦs were cultured in the presence of the 2 mM SAPs (<CGC) supplemented in the cell culture medium for 48 hours. Quantitative analysis of cell surface markers of* ***(B)*** *HLA-DR,* ***(C)*** *CD105,* ***(D)*** *CD163 for all SAPs. Geometric mean fluorescence intensity (gMFI) was plotted. Black line and error bar in the plot represent mean and standard deviation, respectively.* ***(E-G)*** *Cytokine secretion profile using multiplex bead-based ELISA. Significant changes were found only in 3 cytokines presented here:* ***(E)*** *TNF-α* ***(F)*** *IL-1β* ***(G)*** *IL-10, for all SAPs. In all cases* ***(A-G)****, horizontal dashed lines depict median values for the control MΦs with different polarization states obtained as indicated in methods section. Statistical analysis in* ***B-G*** *was done by Kruskal-Wallis multiple comparisons test. A statistically significant results were considered for p<0.05 (* - <0.05, ** - <0.01, *** - <0.005 and **** - <0.001).*

In first instance we decided to screen our family of SAPs prepared <CGC (at 2 mM, liquid) with genetically similar monocytic THP-1 cells. These cells enable rapid screening of the immunomodulatory potential by minimizing any biological variability stemming from primary human cells, thereby ensuring any differences between response indeed come from the influence of the SAPs. In first instance we directly tested whether SAPs have any capacity to activate NFκB signalling pathway, well correlated with the induction of pro-inflammatory responses,[15, 64] directly on THP-1 monocytic cells with the NFκB-GFP reporter gene (***Figure S6A***). None of the SAPs triggered activation of this inflammatory pathway. This response was the same as to the untreated control and cells treated with IFN-γ, which is known not to trigger this pathway. Across all tested samples, only when cells treated with TNF-α activated this pathway (***Figure S6A***).[65] Based on the absence of obvious inflammatory response, we then aimed to confirm the general polarization capacity and tested it for all SAPs against THP-1-derived MΦs following the protocol established by Sapudom *et al.* (***Figure 6A***).[66] First, MΦ phenotypes were characterized using their specific surface markers, namely, HLA-DR for pro-inflammatory macrophages (M1) and CD105 for anti-inflammatory macrophages (M2) by flow cytometry.[10] We observed significantly higher abundance of HLA-DR surface markers for cells encapsulated with **YEF8** (***Figure 6B***), indicating its pro-inflammatory polarization capacity. On the other hand, we noticed high abundance of $CD105^+$ cells when encapsulated with control **EF8** SAP (***Figure 6C***), indicating cell polarization towards M2 phenotype.[10] The obtained subtypes correspond well to the control M1 and M2 types, presented in all graphs as horizontal lines. Importantly, none of the other SAPs appeared to have significant expression of these cell surface markers, and hence do not trigger any obvious pro- or anti-inflammatory response in this model, under the tested conditions. Given the importance of the M2 subtypes in tissue resolution, next we evaluated specific surface receptors, including CD206 and C163, known to be associated with M2a and M2c subtypes, respectively.[10, 67] Interestingly, no significant differences were found for CD206 receptors between all SAPs (***Figure S6B***), whereas

highest abundance of $CD163^+$ was found when encapsulated with **EF8** SAP (***Figure 6D***). This indicates **EF8** peptide may stimulate the MΦs towards a tissue repair state, promoting the healthy restoration of normal architecture.[68]

We further studied the secretion profiles of 13 most common cytokines released by MΦs using multiplex bead-based ELISA: IL-4, IL-2, CXCL10 (IP-10), IL-1β, TNF-α, CCL2 (MCP-1), IL-17A, IL-6, IL-10, IFN-γ, IL-12p70, CXCL8 (IL-8), and TGF-β1. Significant changes were found in three of the tested cytokines: pro-inflammatory - TNF-α (***Figure 6E***) and IL-1β (***Figure 6F***), and anti-inflammatory - IL-10 (***Figure 6G***). Again, **YEF8** SAP exhibited largest amounts of released pro-inflammatory factors (TNF-α and IL-1β) compared to all other SAPs, and similar in the level to control M1 (***Figure 6E-F***), confirming flow cytometry data. **YEF8Y** and **EYF8** SAPs had slightly elevated release of IL-1β compared to **EF8** ($p<0.05$), however values were significantly lower compared to the control M1 (***Figure 6F***). No noticeable changes were seen in TNF-α expression (***Figure 6E***). **EF8** SAP induced highest release of IL-10, an important cytokine for the remodelling of external matrix by MΦ, thus confirming polarization towards M2c subtype.[10, 69] The final MΦ fate is driven by the complex interplay between external environmental signals and hardwired differentiation programming capabilities. Given the observed opposed functional polarizations states of MΦ between **EF8** (M2c) and **YEF8** (M1) SAPs, we hypothesize that the underlying nanostructure or edge-driven chemical moieties could be responsible for the initiation of this function, as demonstrated in previous sections. The role of viscoelasticity of bulk hydrogels in that modulation can be decoupled from the seen effects, as here we used the soluble nanostructures at a concentration of 2 mM (<CGC) before any gelation occurs. Wang and Bratlie provided guidelines for MΦ polarization as a function of used polymer chemistry properties.[70] They argued that chemistry leading to more H-bonding capacity and higher hydrophilicity stimulates MΦ towards M1 state, whereas overall charge plays a role in M2 modulation. Our findings suggest that in the case of **YEF8** SAP, in principle the tyrosine placed in first position may enable additional H-bonding and contribute to

polarization of M1 state compared to **EF8**. However, noticing lack of such induction for other Y-containing SAPs seems to indicate the nanostructure type (rod-like ribbons) as the putatively prevalent factor in this polarization.

5. Immunological effects exerted on clinically relevant PMBCs-derived MΦs.

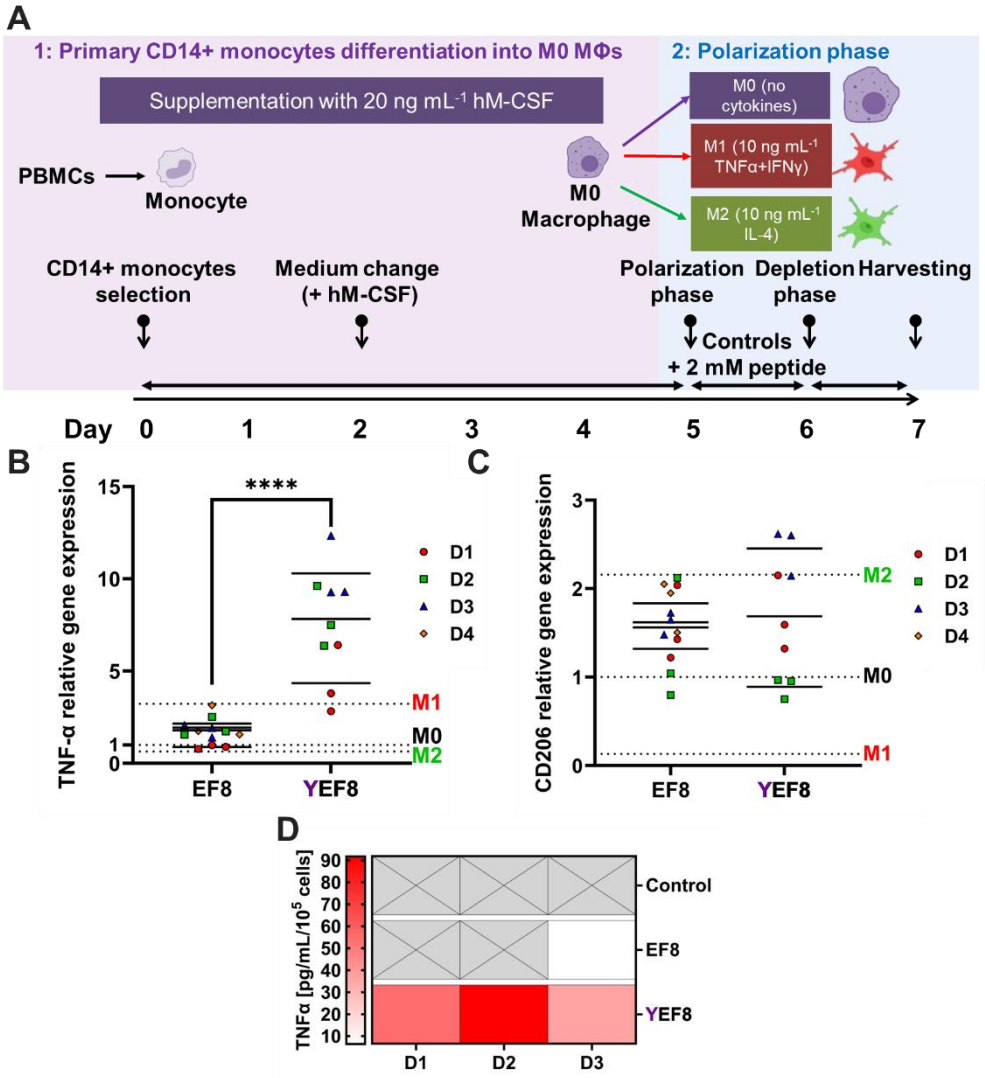

Figure 7. (A) Differentiation protocol and subsequent characterisation of peripheral blood mononuclear cells *(PBMCs)-derived MΦs. PBMCs were differentiated into M0 macrophages over 5 days period by supplementation with 20 ng mL^{-1} human macrophage colony-stimulating factor (hM-CSF). At day 5, differentiated M0 macrophages were polarized by medium supplemented with 10 ng mL^{-1} TNF-α and IFN-γ towards an M1 state (M1 control) and 10 ng mL^{-1} IL-4 towards an M2 state (M2 control) for 24 hours, followed by a 24-hour rest in medium without cytokines. Untreated M0 MΦs were treated as a control samples and cultured in medium without any cytokines. The same three polarization states were maintained (M0, M1, M2), either without any external influence of materials (control), or in the presence of the 2 mM SAPs supplemented in the cell culture medium at day 5 (for 24 hours). Gene expression of* ***(B)*** *TNF-α and* ***(C)*** *MRC1 (CD206) measured by RT-qPCR for untreated MΦs encapsulated with 2 mM of* ***EF8*** *or* ***YEF8*** *SAPs. Gene expression is represented*

as fold change compared to RPLP0 (a housekeeping gene) of the M0 untreated control group per each donor (n=3). Horizontal dashed lines depict average values across all donors for the control MΦs with different polarization states. Analysis by two-way ANOVA with Tukey's multiple comparisons test. A statistically significant results were considered for p<0.05 (- <0.05, ** - <0.01, *** - <0.005 and **** - <0.001).* ***(D)*** *TNF-α secretion measured by ELISA for cells treated with 2 mM SAPs (represented in rows) with the same conditioning as described in parts* ***D****. Grey crossed boxes indicate measurements below the limit of detection.*

Next, to confirm and assess clinical viability of the unique polarization capacity of **EF8** and **YEF8** SAPs, we used an established protocol of peripheral blood mononuclear cells (PBMCs)-derived MΦs[44] (***Figure 7A***) from 5 human donors and evaluated TNF-α/CD206 gene expression (***Figure 7B-C*** and ***Figure S7A-B***) and released TNF-α cytokine (***Figure 7D*** and ***Figure S7C***). As expected, averaging from all donors, TNF-α was typically upregulated in M1 control and downregulated in M2 control (***Figure 7B*** and ***Figure S7A***), whereas CD206 was downregulated in M1 control and upregulated in M2 control (***Figure 7C*** and ***Figure S7B***). When using primary cells, variation across donors is standard.[71] Patient-derived cells bring in a huge variety of environmental and genetic factors, including gender, life style, cholesterol levels, co-morbidities to name a few.[72] Despite these challenges, data from primary cells increase the clinical relevance of our findings. Therefore, within the experimental variations, the overall results confirm previous observations, i.e. the upregulation of TNF-α (***Figure 7B***) and downregulation of CD206 in 2 donors in the M2 tested group (***Figure S7B***) for **YEF8** SAP. This also correlated well with the eleveted levels of TNF-α detected almost exclusively for the **YEF8** SAP (***Figure 7D*** and ***Figure S7C***). Grey boxes in ***Figure 7D*** indicate levels of TNF-α were below the limit of detection.

In general, for the **EF8** SAP, we observed most of measurements falling closer to M0 control in TNF- α gene expression (***Figure 7B*** and ***Figure S7A***) and slight tendency towards M2 in CD206 gene expression (***Figure 7C*** and ***Figure S7B***). No noticeable expression of TNF-α were observed in ELISA measurements for this SAP (***Figure 7D*** and ***Figure S7C***). These results confirms the phenotype of THP-1 derived MΦs in section 4 holds true for MΦs directly differentiated from PBMCs

across multiple tested donors, and brings a critical role of the **EF8** sequence as a possible orchestrator balancing repair of tissues, such as e.g. in wound healing[10] or tendon repairs.[73] In general, two other tested SAPs, **EF8Y** and **EYF8**, showed downregulation of TNF-α (***Figure S7A***), upregulation of CD206 (***Figure S7B***) in M0 groups, indicating possible MΦs polarization towards M2a-like state. Although this observation is contrasting THP-1 cells-derived MΦs behaviour in section 4 and potentially depicts differences between the two types of cell sources, the conclusions from these two studies still indicate that these SAPs do not induce any significant inflammatory response compared to the **YEF8.** Unfortunately the effects of **YEF8Y** SAP could not be evaluated due to noticed interference of this SAP with the RNA extraction process. Nevertheless, the secreted TNF-α protein levels for **EF8Y**, **EYF8** and **YEF8Y** were virtually negligible (***Figure S7C***), confirming the lack of pro-inflammatory response from these SAPs and their non-immunogenecity.

Conclusions

In this work we designed five β-sheet forming self-assembling peptide sequences: EFEFKFEFK (**EF8**), YEFEFKFEFK (**YEF8**), YEFEFKFEFK (**EF8Y**), YEFEFKFEFK (**YEF8Y**) and EYEFKFEFK (**EYF8**) (F: phenylalanine; E: glutamic acid; K: lysine, **Y**: tyrosine). We then investigated the role of repositioning the tyrosine residue on the self-assembly, gelation and immunological function of macrophages derived from two discrete cell sources. Our results showed that the addition of tyrosine did not affect the ability of the peptides to form β-sheet-rich nanofibers. Titrations of peptides revealed that all SAPs carry a charge in the range $-2 \leq Z \leq -1$ at physiological pH (7.2 ± 0.2) and all form self-supporting hydrogels above similar CGC ~2.5 mM. The only exception was **YEF8**, which retained cloudiness at this pH when bulk hydrogels were formed. Furthermore, in bulk hydrogel form at 20 mM, all SAP hydrogels were characterized by similar storage modulus profile in the range 3.4 ± 2.8 kPa, were shear-thinning, injectable and freeform 3D printable in an embedded bath. **YEF8** was characterized by larger variability in storage

modulus, correlating well with its self-assembly to larger rod-like flat ribbon nanostructures (>20 nm). Sequences **EF8Y**, **YEF8Y**, **EYF8** self-assembled into thin nanofibers $d \approx 3.8 \pm 0.2$ nm, **YEF8** self-assembled into rod-like flat ribbons $d > 20$ nm and **EF8** (control) consisted of both types of self-assembled structures with the prevalence of thin nanofibers. The nanostructure form of SAP correlated very well with the response of MΦs derived from genetically similar monocytic model THP-1 cells and donor genetically variable peripheral blood mononuclear cells (PBMCs). Presence of soluble **EF8** nanofibers (at 2 mM) induced a strong anti-inflammatory response and polarization towards M2a and M2c MΦ states, indicating this SAP as a possible modulator of the tissue repair. **YEF8** SAP displayed tendency for inducing strong pro-inflammatory response and polarization towards M1 MΦ phenotype, whereas the **EF8Y**, **YEF8Y**, **EYF8** SAPs did not induce strong inflammatory responses in our models. Since immunomodulation towards a certain state offers the opportunity to enhance functional recovery, here we provide a family of SAPs that can be used as nanobiomaterial immuno-modulators. By minor variation of position of tyrosine in the sequence, nanostructures with tendency towards anti-inflammatory, pro-inflammatory, or non-immunogenic property were designed. These responses seem to be linked to the type of nanostructure formed, as well as possible H-bonding edge-interactions stemming from the edges of these nanostructures. There are reports that this family of SAPs can be uptaken by cells,[74] and thus one of the alterantive mechanisms might involve internal signalling after endocytosis of the neighbouring nanofibers/nanorods, however deciphering exact mechanisms of this polarization remains to be investigated in the future studies. Our work brings basic physicochemical rules for the design of future translational immunomodulatory SAPs nanobiomaterials that could be used for reprogramming of immune system towards desired reparative, or inflammation-induced states.

Materials and methods

Materials: Peptides were purchased as HCl salts form Biomatik Corporation (Wilmington, DE, Canada) and used as received. The peptide sequence purity was confirmed using reverse phase high-performance liquid chromatography (HPLC) and was >92%. All solvents and reagents were purchased from Sigma-Aldrich and used as received.

Theoretical charge and experimental titrations: The theoretical net charge of different peptide sequences at each pH value was calculated by the following equation:

$$Z = \sum_i N_i \frac{10^{pK_{a_i}}}{10^{pH} + 10^{pK_{a_i}}} - \sum_j N_j \frac{10^{pH}}{10^{pH} + 10^{pK_{a_j}}} \qquad \textit{(Equation 1)}$$

, where $N_{i/j}$ are the numbers of functional groups present on peptide, and $pK_{ai/j}$ the pK_a are the basic (i - $pK_a > 7$) and acidic (j - $pK_a < 7$) values, respectively.[20] Peptide titrations experiments were performed by addition of a 0.05 M NaOH solution in 5 µL steps to a 1 mL miliQ water (H_2O) peptide solution with a ~1 mM starting peptide concentration. After each NaOH addition, the samples were vigorously agitated using a vortexer to ensure homogenous mixing and the pH was measured using an 827 Metrohm pH Meter (Metrohm AG, Switzerland). The experiments were repeated at least 2 times.

Hydrogel preparation: Typically, for the preparation of 1 mL volume of the 20 mM hydrogel, the required amount of peptide powder was first dissolved in 700 µL of miliQ H_2O. To ensure full and homogeneous dissolution, the samples were then sonicated at 80 kHz for 30 min in an ice bath (to ensure low temperature). Hydrogels were then prepared by adjusting the pH of the peptide solutions to the desired value through stepwise addition of a 0.5 M NaOH solution. After each addition, the samples were vigorously agitated using a vortexer to ensure homogeneous mixing. If bubbles were present after mixing, gentle centrifugation (at 4000 rpm for 1 minute) was used to remove them. Concentrations and volumes were scaled as needed for each experiment.

Transmission Electron Microscopy (TEM): Peptide hydrogels were prepared at 20 mM concentration as described above and diluted 100-fold using deionised H_2O. The samples were then

gently pipetted up and down for 60 seconds, followed by 60 seconds vortexing and sonication at 35 kHz at room temperature in normal mode for 3 min. A carbon film coated 300 Mesh copper grid (Electron Microscopy Sciences, CF300-CU-50) was placed sequentially on a 10 µL sample droplet for 60 s. The sample was then blotted and a 10 µL droplet of Uranyless solution was applied for 60 s, blotted, and then rinsed using H_2O until finally left to dry for 5 min. TEM images were taken using a Hitachi TEM H800 transmission electron microscope running at 100 keV. A minimum of 100 nanofibers and nanofiber bundle widths were measured manually using ImageJ software for each peptide system.

Small-Angle X-ray Scattering: SAXS experiments were performed on beamline B21 at the diamond light source (DLS) synchrotron (Didcot, UK), following setup previously described.[75] Briefly, the energy of the beam was 13.05 keV, corresponding to an X-ray wavelength of 0.95 Å. The sample-to-detector distance was fixed to 3.7 m corresponding to an accessible momentum transfer vector range of 0.03 $nm^{-1} < q = (4\pi/\lambda) \sin(\theta/2) < 3.4$ nm^{-1}, where θ is the scattering angle and λ the wavelength of the incident photons. Calibration of the SAXS detector (Eiger 4M, Dectris, Switzerland) was performed using silver behenate powder. Samples were collected at 20 ºC for 20 consecutive framers at the exposure time of 1 s each. The samples were prepared as described above at 20 mM, and subsequently diluted to lower concentrations of 10, 5 and 2.5 mM prior to measurements. pH was checked after each dilution to ensure the original pH was unaffected by the dilution process. Such prepared hydrogels were left on the agitator for 4 hours at room temperature to ensure complete homogeneity.. Samples were measured either in an empty Kapton tape, or in quartz capillaries (1.5 mm outer diameter and 0.01 mm wall thickness) from Capillary Tube Supplies Ltd (Bodmin, UK). These were respectively For Kapton tapes, used as background, they were subtracted from all spectra and data were reduced using ScatterIV (Rambo, R. P. (2017). For samples placed in capillaries, an empty capillary was used as the background and subtracted from all spectra, and data were reduced using the Dawn software suite available from DLS. The 2D scattering patterns were integrated using

azimuthal integration to generate the 1D scattering patterns. Fitting cylinders (right circular cylinder with uniform scattering length density function) was done using SasView 5.0.6 software (http://www.sasview.org/). The 5 mM **YEF8Y** sample was not measured properly during beamtime due to the Arinax sample change robot fail to pick and load it up during automated measurements (based on the resulting spectra of an empty capillary). Hence, we could not analyse this concentration in the analysis provided in section 2. 5 mM **EYF8** was the only sample for which consecutive radiation damage was noticed, hence it was excluded from the analysis/presentation.

Attenuated Total Reflectance−Fourier Transform Infrared Spectroscopy (ATR-FTIR): Hydrogels or solutions were spread as prepared onto the crystal surface of a Bruker Tensor 27 spectrometer equipped with a diamond multibounce attenuated total reflectance (ATR) plate. The transmittance spectra were recorded (256 scans) between 4000 and 400 cm^{-1} with a resolution of 2 cm^{-1}. MiliQ H_2O was used as background and was automatically subtracted from the recorded spectra using the OPUS software provided with the instrument.

Rotational and oscillatory Rheology: Rheological studies were carried out on an Anton Paar MCR-302 rheometer (Anton Paar GmbH, Austria). All measurements were taken with a gap size of 0.5 mm and a parallel plate with a diameter of 25 mm. Samples were prepared as described above. Hydrogels were gently spread onto the rheometer's static bottom plate and the rheometer top plate lowered to the desired gap size. To prevent sample drying during the measurements, silicone oil was applied around the plate to seal the hydrogel. Samples were left to equilibrate for 180 s and then frequency sweeps were assessed at a temperature of 37 °C, with a strain of $\varepsilon = 0.2\%$. Amplitude sweeps were performed in an oscillatory mode at a constant frequency of f = 1 Hz at 37 °C, with strain varied from 0.01 to 1000%. All viscosity-shear rate experiments (flow curves) were performed at 37 °C, with samples subjected to shear rate from 0.01 to 1000 s^{-1}, and being held at each shear rate until a stable reading was reported by the instrument. The shear thinning behaviour was characterised by fitting the Power Law equation (1) to the linear region of the shear rate-viscosity rheology plot.

$$\eta = K\dot{\gamma}^{n-1} \qquad \textit{(Equation 2)}$$

where η is the viscosity, $\dot{\gamma}$ the shear rate, K a consistency value and n the shear thinning exponent. Flow recovery tests in a rotational mode were performed by initially subjecting sample to shear close to a zero-shear value (0.01 s^{-1}) for 200 seconds. Then shear rate was increased to 895 s^{-1} and kept for 100 seconds. Recovery was then monitored for 200 seconds by switching the shear rate back to 0.01 s^{-1}, and the same cycle was repeated. The oscillatory recovery experiments were performed by applying sequentially low (0.2%) and high shear strain (100%) in 10 min intervals over 2 cycles. All recovery tests were performed at 37 °C. All measurements were repeated at least two times, and average and standard deviation presented.

Freeform 3D printing: For embedded printing, we prepared microgel bath from 0.8% (w/v) Carbopol® 940 (Acros Organics Geel, Belgium) printing bath following previous protocols.[76] Briefly, 0.20 g of Carbopol® 940 was dissolved in 20 mL of MiliQ H_2O and prior to printing, the pH of the bath was adjusted to 7.2 ± 0.2 with 2M sodium hydroxide (NaOH). The Carbopol bath was stored at 4 °C until printing. 1 mL of bath per well was deposited into 24-well plates and degassed using an Eppendorf centrifuge at 500 g for 5 min. Freeform 3D printing was then performed using a 3D Discovery™ Printer and BioCAD software (version 1.1-12) from RegenHu Ltd. (Villaz-St-Pierre, Switzerland) using a 20G needle with PTFE- with 0.61 mm (Nordson EFD, Westlake, USA). 3 mL of SAP hydrogels **EF8** and **EYF8** where prepared at 20 mM concentration prior to printing as per procedure above, with the addition of 20 µL of 10 mg mL^{-1} Coomassie Brilliant Blue R250 dye to enable easier visualization of printed structures. SAP inks were loaded into 3cc printing cartridges, which were either centrifuged at 1000 rcf for 5 minutes before printing (presented in ***Figure 5C-D***) or centrifuged at 3220 rcf for 5 minutes before printing (presented in ***Figure S5B-C***). SAP inks were deposited at a height of 2 mm above the bottom inside the Carbopol bath at a velocity of 0.5 mm s^{-1}, and with a pressure of 0.5 – 1 bar. The printed structures were 3 circles vertically spaced by 1 mm in

3 separate wells. Printing was done at 23-25 °C range of ambient temperature, and 12-25% relative humidity.

Quantification of the pro-inflammatory response of monocytes via NFKB expression: THP-1 monocytic cells with the NFκB-GFP reporter gene were kindly provided by Dr. Xin Xie (Core Technology Platform, New York University Abu Dhabi, UAE). The cells were cultured in RPMI-1640 media supplemented with 10% fetal bovine serum (FBS), 1% sodium pyruvate, 0.01% mercaptoethanol, and 1% penicillin/streptomycin at 37°C, 5% CO_2, and 95% humidity. Cell culture media and supplements were purchased from Gibco™ (Thermo Fisher Scientific, Inc., Dreieich, Germany). To quantify the pro-inflammatory response, 5×10^5 cells were cultured with or without SAPs prepared at 2 mM (<CGC) for 24 hours under standard cell culture conditions. As a positive control, the cells were treated with 10 ng mL^{-1} TNF-α (Biolegend, San Diego, CA, USA), known to activate NFκB signalling. Cells were also treated with 10 ng mL^{-1} IFN-γ, as it is a known to confirm specificity of control because it does not trigger NFkB signalling pathway. Subsequently, the cells were analysed using an Attune NxT Flow Cytometer equipped with an autosampler (Thermo Fisher Scientific, Inc., Dreieich, Germany). Data analysis was performed using FlowJo software (Becton, Dickinson and Company, Franklin Lakes, NJ, USA). The geometric mean fluorescence intensity (gMFI) of the NFκB-GFP reporter was evaluated. Experiments were performed in quadruplicate.

Macrophage differentiation from THP-1 cells and treatment with the SAPs: For macrophage differentiation, 1×10^5 THP-1 cells (ATCC, Manassas, VA, USA) were incubated with 300 nM phorbol 12-myristate 13-acetate (PMA; Sigma-Aldrich, Darmstadt, Germany) in RPMI-1640 media supplemented with 1% sodium pyruvate, 0.01% mercaptoethanol, and 1% penicillin/streptomycin but without fetal bovine serum (FBS), following previously published protocols.[66, 68] The cell culture media and supplements were acquired from Gibco™ (Thermo Fisher Scientific, Inc., Dreieich, Germany). After 6 hours, the differentiation medium was removed, and the cells were allowed to rest for 24 hours in RPMI-1640 without FBS and PMA. Subsequently, the differentiated macrophages

were cultured either with or without self-assembling peptides (SAPs) prepared at 2 mM for 48 hours. As a control, macrophages were activated into pro-inflammatory (M1) macrophages for 48 hours by adding 10 pg mL^{-1} lipopolysaccharide (LPS; Sigma, USA) and 20 ng mL^{-1} interferon-gamma (IFN-γ; Biolegend, San Diego, CA, USA). For anti-inflammatory activation, macrophages were induced into the M2a subtype with 20 ng mL^{-1} interleukin 4 (IL-4; Biolegend, USA) and 20 ng mL^{-1} interleukin 13 (IL-13; Biolegend, USA), or into the M2c subtype with 20 ng mL^{-1} interleukin 10 (IL-10; Biolegend, USA).

Quantitative analysis of THP-1 derived macrophages (MΦs) cell surface markers and their cytokine secretion profile: For analysis of macrophage cell surface markers, macrophages were detached from the cell culture plates using Macrophage Detachment Solution DXF (PromoCell, Heidelberg, Germany) following incubation with 2 mM SAPs. Before cell staining, they were incubated with Human TruStain FcX™ – Fc Receptor Blocking Solution (5 µL of blocking solution in 1000 µL of staining volume; Biolegend, San Diego, CA, USA) for 5 minutes under standard cell culture conditions. Subsequently, the cells were stained with mouse anti-human HLA-DR (clone: L243) conjugated with Brilliant Violet 421, CD163 (Clone: GHI/61) conjugated with PE-Cy7, mouse anti-human CD206 (Clone: 15-2) conjugated with Brilliant Violet 510, and DRAQ7 (a cell viability staining dye) for 30 minutes on ice. The antibodies and DRAQ7 dye were diluted in PBS at a 1:250 ratio. All antibodies used in this study were sourced from Biolegend, San Diego, CA, USA. The stained cells were then analysed using an Attune NxT Flow Cytometer equipped with an autosampler (Thermo Fisher Scientific, Inc., Dreieich, Germany), with compensation settings adjusted prior to analysis. Data analysis was conducted using FlowJo software (Becton, Dickinson and Company, Franklin Lakes, NJ, USA), focusing on the geometric mean fluorescence intensity of the cell surface markers. Experiments were performed in 5 replicates. For cytokine secretion profile analysis, cell culture supernatants were harvested following incubation with SAPs products. The cytokine levels were quantified using a bead-based multiplex immunoassay (LEGENDplex™ Human Essential

Immune Response Panel; Biolegend, San Diego, CA, USA) designed for IL-4, IL-2, CXCL10 (IP-10), IL-1β, TNF-α, CCL2 (MCP-1), IL-17A, IL-6, IL-10, IFN-γ, IL-12p70, CXCL8 (IL-8), and TGF-β1, according to the manufacturer's protocol. The samples were analysed on an Attune NxT Flow Cytometer (Thermo Fisher Scientific, Carlsbad, CA, USA). Data were processed using a 5-parameter curve fitting algorithm with LEGENDplex™ data analysis software (Biolegend, San Diego, CA, USA), and experiments were performed in 5 replicates.

Peripheral blood mononuclear cells (PBMCs)-derived macrophages (MΦs) cell culture: Primary human monocytes were isolated from buffy coats purchased from the Regional Blood Donation Service SRK Graubünden (Chur, Switzerland) from five human donors (abbreviated as D1, D2, D3, D4 and D5) using Ficoll density gradient separation. Obtained peripheral blood mononuclear cells (PMBCs) were labelled with CD14 magnetic beads followed by magnetic-activated cell sorting.[77] $CD14^+$ monocytes cells were resuspended in RPMI medium supplemented with 10% FBS and then seeded onto tissue culture plastic at a density of 3×10^5 cells $well^{-1}$ in the presence of 20 ng mL^{-1} human macrophage colony-stimulating factor (hM-CSF) for 5 days, similarly to our previous protocol.[44] Medium (still containing hM-CSF) was exchanged on day 2 (see ***Figure 7A*** for timing). At day 5, hM-CSF-free medium was supplemented with 10 ng mL^{-1} TNF-α and 10 ng mL^{-1} IFN-γ for M1 MΦs and 10 ng mL^{-1} IL-4 for M2 MΦs for 24 hours followed by a 24-hour rest in medium without cytokines (see ***Figure 7A*** for timing). Control samples (M0 MΦs) were cultured in medium without any cytokines. Furthermore, on day 5, the same three polarization states were maintained (M0, M1, M2), either without any external influence of materials, or in the presence of the 2 mM SAPs supplemented in the cell culture medium. Noteworthy, 2 mM of all SAPs was below CGC to maintain the supplementation of nanostructure form (<CGC, solution form) and did not result in a formation of any self-supporting physical hydrogels. On day 7, conditioned medium was collected for ELISA, whereas samples were washed two times with PBS and stored in TRI-reagent for subsequent RNA isolation.

Enzyme-linked immunosorbent assay (ELISA): At the end of each polarization experiment, supernatant media was collected and kept for measurements of pro-inflammatory (IL-6, TNF-α) and anti-inflammatory (CD163, IL-10, IL-12) cytokines, associated with M1 and M2 MΦs, respectively. The DuoSet ELISA systems were used according to the manufacturer's instructions of DY210 (TNF-α) R&D Systems. Absorbance values were measured on Infinite® 200 Pro plate reader (Tecan, Männedorf, Switzerland) at 450 nm with a background wavelength correction of 540 nm.

RNA isolation and RT-qPCR gene analysis: To assess the polarization of macrophages, cells were collected and seeded in a 24-well plate at a concentration and with treatments described above. RNA was isolated with salt precipitation and TaqManTM Reverse Transcription Kit was used to generate cDNA. Relative gene expression reactions were set up in 10 µL reaction mixes using TaqManTM MasterMix, relevant human primers (***Table 1***), diethyl pyrocarbonate treated water (DEPC-water) and cDNA. Real-time polymerase chain reaction (real-time PCR) was performed on two technical replicates for n=3 repeats, using QuantStudio 7 Flex. The relative gene expression was identified using $2^{-\Delta\Delta Ct}$ value with RPLP0 as endogenous control and positive control (M0 MΦs, no supplemented material or cytokines) were used for normalization. Normalization was performed per each donor, i.e. all relative expression is normalized to M0 untreated control group of each donor.

Table 1. Human primer sequences for real-time PCR.

Marker	Assay ID (THERMOFISHER)	Role
TNF-α	Hs00174128_m1	Pro-inflammatory marker (associated with M1 MΦs)
MRC1 (CD206)	Hs00267207_m1	Surface marker for M2 MΦs
RPLP0	Forward: *5'-TGG GCA AGA ACA CCA TGA TG-3'* Reverse: *5'-CGG ATA TGA GGC AGC AGT TTC-3'* Probe: *5'-AGG GCA CCT GGA AAA CAA CCC AGC-3'*	Housekeeping gene

Statistical analysis: All results were analysed and presented with GraphPad Prism version 9.3.1. Results are shown as an average ± standard deviation (SD), with individual points marked. To perform statistical significance one-way analysis of variance (ANOVA) with Šídák's multiple comparisons, Tukey's multiple comparisons test, or Kruskal-Wallis multiple comparisons were used

and noted in each case in Figure description. A statistically significant results were considered as of $p<0.05$ (ns - >0.05, * - <0.05, ** - <0.01, *** - <0.005 and **** - <0.001).

Schemes: ***Figure 1A-B*** and graphical abstract were created with BioRender.com.

Author Contributions

J.K.W.: Conceptualization, data curation, formal analysis, funding acquisition, investigation, methodology, project administration, resources, supervision, validation, visualization, writing - original draft, writing – review & editing; **E.I.B.**: Data curation, investigation, methodology, writing – review & editing; **A.J.V.**: Data curation, investigation, methodology, writing – review & editing; **M.M.**: Data curation, investigation, methodology, writing – review & editing; **M.A.**: Data curation, investigation, methodology, writing – review & editing; **P.S.T.**: Data curation, methodology; **J.S.** Data curation, investigation, methodology, formal analysis, writing – review & editing; **J.T.** Conceptualization, resources, funding acquisition, supervision, writing – review & editing; **D. E.**: Conceptualization, resources, funding acquisition, supervision, writing – review & editing; **M.D.**: Conceptualization, funding acquisition, resources, methodology, project administration, resources, supervision, writing – review & editing.

Funding sources

This work was supported by the European Union's Horizon 2020 (H2020-MSCA-IF-2019) research and innovation programme under the Marie Skłodowska-Curie grant agreement 893099 — ImmunoBioInks and by the Leading House for the Middle East and North Africa for Research Partnership Grant 2022 "Space ImmunoBioInks" (RPG-2022-38). J.K.W. is also grateful to DLS (Didcot, UK) for awarding beam time (SM29767) to this project. J.K.W and M.D'E also acknowledge the European Union's Horizon 2020 research and innovation programme under the grant agreement No 857287 (BBCE) as well as funding provided by AO Foundation.

Acknowledgements

The authors thank Nicolas Devantay for his technical support and Dr. Ursula Menzel for her assistance with PCR plating. D.E. thank the Nora Mallouk-Forges of the Centre de Microscopie Electronique Stéphanois for technical support. The authors would also like to acknowledge support from Molecular and Cell biology core technology platform at New York University Abu Dhabi. This work benefited from the use of the SasView application, originally developed under NSF award DMR-0520547. SasView contains code developed with funding from the European Union's Horizon 2020 research and innovation programme under the SINE2020 project, grant agreement No 654000.

Supplementary data

Supplementary data available: Photographs of gelation of all SAP hydrogels; Normalized ATR-FTIR spectra, Amplitude and Frequency sweeps of all SAP hydrogels; Oscillatory rheology recovery of tyrosine containing SAP hydrogels and supporting digital photographs of printed rings in other conditions. Additional immunological data (flow cytometry, PCR) for macrophage polarization studies.

Conflicts of interest

There are no conflicts to declare.

Notes

All research data supporting this publication are directly available within this publication and associated supporting information.

ORCID numbers of authors:

Jacek K. Wychowaniec: https://orcid.org/0000-0002-6597-5242

Ezgi Irem Bektas: https://orcid.org/0000-0002-3700-5708

Andrea J. Vernengo: https://orcid.org/0000-0002-5143-7435

Marcia Mürner: https://orcid.org/0009-0006-5305-2113

Marielle Airoldi: https://orcid.org/0009-0006-0311-3109

Paul Sean Tipay: https://orcid.org/0009-0002-9790-2598

Jiranuwat Sapudom: https://orcid.org/0000-0001-6627-7713

Jeremy Teo: https://orcid.org/0000-0001-6869-3833

David Eglin: https://orcid.org/0000-0002-8500-6887

Matteo D'Este: https://orcid.org/0000-0002-0424-8172

References

(1) Mao, J.; Chen, L.; Cai, Z.; Qian, S.; Liu, Z.; Zhao, B.; Zhang, Y.; Sun, X.; Cui, W. Advanced Biomaterials for Regulating Polarization of Macrophages in Wound Healing. *Advanced Functional Materials* **2021**, *32* (12), 2111003. DOI: 10.1002/adfm.202111003.

(2) Minton, K. Stress-induced macrophage polarization. *Nature Reviews Immunology* **2017**, *17*, 277. DOI: 10.1038/nri.2017.41. Bucher, C. H.; Schlundt, C.; Wulsten, D.; Sass, F. A.; Wendler, S.; Ellinghaus, A.; Thiele, T.; Seemann, R.; Willie, B. M.; Volk, H.-D.; et al. Experience in the Adaptive Immunity Impacts Bone Homeostasis, Remodeling, and Healing. *Frontiers in Immunology* **2019**, *10*, 797, 10.3389/fimmu.2019.00797. Zhang, B.; Su, Y.; Zhou, J.; Zheng, Y.; Zhu, D. Toward a Better Regeneration through Implant-Mediated Immunomodulation: Harnessing the Immune Responses. *Advanced Science* **2021**, *8* (16), 2100446, https://doi.org/10.1002/advs.202100446. DOI: https://doi.org/10.1002/advs.202100446 (acccessed 2021/10/11). Shan, B.; Wang, X.; Wu, Y.; Xu, C.; Xia, Z.; Dai, J.; Shao, M.; Zhao, F.; He, S.; Yang, L.; et al. The metabolic ER stress sensor IRE1alpha suppresses alternative activation of macrophages and impairs energy expenditure in obesity. *Nat Immunol* **2017**, *18* (5), 519-529, Article. DOI: 10.1038/ni.3709 From NLM Medline.

Paludan, S. R.; Pradeu, T.; Masters, S. L.; Mogensen, T. H. Constitutive immune mechanisms: mediators of host defence and immune regulation. *Nature Reviews Immunology* **2021**, *21* (3), 137-150. DOI: 10.1038/s41577-020-0391-5.

(3) Rust, R.; Kaiser, J. Insights into the Dual Role of Inflammation after Spinal Cord Injury. *The Journal of neuroscience : the official journal of the Society for Neuroscience* **2017**, *37* (18), 4658-4660. DOI: 10.1523/JNEUROSCI.0498-17.2017 PubMed. David, S.; Kroner, A. Repertoire of microglial and macrophage responses after spinal cord injury. *Nat Rev Neurosci* **2011**, *12* (7), 388-399. DOI: 10.1038/nrn3053 From NLM.

(4) Gensel, J. C.; Zhang, B. Macrophage activation and its role in repair and pathology after spinal cord injury. *Brain Research* **2015**, *1619*, 1-11. DOI: https://doi.org/10.1016/j.brainres.2014.12.045. Kigerl, K. A.; Gensel, J. C.; Ankeny, D. P.; Alexander, J. K.; Donnelly, D. J.; Popovich, P. G. Identification of Two Distinct Macrophage Subsets with Divergent Effects Causing either Neurotoxicity or Regeneration in the Injured Mouse Spinal Cord. *The Journal of Neuroscience* **2009**, *29* (43), 13435.

(5) Fang, P.; Li, X.; Dai, J.; Cole, L.; Camacho, J. A.; Zhang, Y.; Ji, Y.; Wang, J.; Yang, X. F.; Wang, H. Immune cell subset differentiation and tissue inflammation. *J Hematol Oncol* **2018**, *11* (1), 97. DOI: 10.1186/s13045-018-0637-x From NLM Medline. Chen, L.; Deng, H.; Cui, H.; Fang, J.; Zuo, Z.; Deng, J.; Li, Y.; Wang, X.; Zhao, L. Inflammatory responses and inflammation-associated diseases in organs. *Oncotarget* **2017**, *9* (6).

(6) Krzyszczyk, P.; Schloss, R.; Palmer, A.; Berthiaume, F. The Role of Macrophages in Acute and Chronic Wound Healing and Interventions to Promote Pro-wound Healing Phenotypes. *Frontiers in Physiology* **2018**, *9*, Review. DOI: 10.3389/fphys.2018.00419.

(7) Arango Duque, G.; Descoteaux, A. Macrophage Cytokines: Involvement in Immunity and Infectious Diseases. *Frontiers in Immunology* **2014**, *5*, Review. DOI: 10.3389/fimmu.2014.00491.

(8) Gordon, S. Alternative activation of macrophages. **2003**, *3* (1), 23-35. Kobashi, S.; Terashima, T.; Katagi, M.; Nakae, Y.; Okano, J.; Suzuki, Y.; Urushitani, M.; Kojima, H. Transplantation of M2-Deviated Microglia Promotes Recovery of Motor Function after Spinal Cord Injury in Mice. *Mol Ther* **2020**, *28* (1), 254-265. DOI: 10.1016/j.ymthe.2019.09.004 From NLM. Ma, S. F.; Chen, Y. J.; Zhang, J. X.; Shen, L.; Wang, R.; Zhou, J. S.; Hu, J. G.; Lü, H. Z. Adoptive transfer of M2 macrophages promotes locomotor recovery in adult rats after spinal cord injury. *Brain Behav Immun* **2015**, *45*, 157-170. DOI: 10.1016/j.bbi.2014.11.007 From NLM.

(9) Lawrence, T.; Natoli, G. Transcriptional regulation of macrophage polarization: enabling diversity with identity. *Nature Reviews Immunology* **2011**, *11* (11), 750-761. DOI: 10.1038/nri3088. Murray, Peter J.; Allen, Judith E.; Biswas, Subhra K.; Fisher, Edward A.; Gilroy, Derek W.; Goerdt, S.; Gordon, S.; Hamilton, John A.; Ivashkiv, Lionel B.; Lawrence, T.; et al. Macrophage Activation and Polarization: Nomenclature and Experimental Guidelines. *Immunity* **2014**, *41* (1), 14-20. DOI: 10.1016/j.immuni.2014.06.008 (acccessed 2023/05/05).

(10) Sapudom, J.; Karaman, S.; Mohamed, W. K. E.; Garcia-Sabate, A.; Quartey, B. C.; Teo, J. C. M. 3D in vitro M2 macrophage model to mimic modulation of tissue repair. *NPJ Regen Med* **2021**, *6* (1), 83. DOI: 10.1038/s41536-021-00193-5 From NLM PubMed-not-MEDLINE.

(11) Xiao, Q.; McAtee, C. K.; Su, X. Phase separation in immune signalling. *Nat Rev Immunol* **2022**, *22* (3), 188-199. DOI: 10.1038/s41577-021-00572-5 From NLM Medline. Lu, J.; Qian, J.; Xu, Z.; Yin, S.; Zhou, L.; Zheng, S.; Zhang, W. Emerging Roles of Liquid-Liquid Phase Separation in Cancer: From Protein Aggregation to Immune-Associated Signaling. *Front Cell Dev Biol* **2021**, *9*, 631486, Review. DOI: 10.3389/fcell.2021.631486 From NLM PubMed-not-MEDLINE.

(12) Walsh, C. M.; Wychowaniec, J. K.; Brougham, D. F.; Dooley, D. Functional hydrogels as therapeutic tools for spinal cord injury: New perspectives on immunopharmacological interventions. *Pharmacol Ther* **2022**, *234*, 108043. DOI: 10.1016/j.pharmthera.2021.108043 From NLM Medline.

(13) Wesdorp, M. A.; Schwab, A.; Bektas, E. I.; Narcisi, R.; Eglin, D.; Stoddart, M. J.; Van Osch, G.; D'Este, M. A culture model to analyze the acute biomaterial-dependent reaction of human primary neutrophils in vitro. *Bioact Mater* **2023**, *20*, 627-637. DOI: 10.1016/j.bioactmat.2022.05.036 From NLM PubMed-not-MEDLINE.

(14) Garcia-Garcia, A.; Pigeot, S.; Martin, I. Engineering of immunoinstructive extracellular matrices for enhanced osteoinductivity. *Bioact Mater* **2023**, *24*, 174-184. DOI: 10.1016/j.bioactmat.2022.12.017 From NLM PubMed-not-MEDLINE.

(15) Sapudom, J.; Kongsema, M.; Methachittipan, A.; Damrongsakkul, S.; Kanokpanont, S.; Teo, J. C. M.; Khongkow, M.; Tonsomboon, K.; Thongnuek, P. Degradation products of crosslinked silk fibroin scaffolds modulate the immune response but not cell toxicity. *J Mater Chem B* **2023**, *11* (16), 3607-3616, 10.1039/D3TB00097D. DOI: 10.1039/d3tb00097d From NLM Medline.

(16) Halperin-Sternfeld, M.; Pokhojaev, A.; Ghosh, M.; Rachmiel, D.; Kannan, R.; Grinberg, I.; Asher, M.; Aviv, M.; Ma, P. X.; Binderman, I.; et al. Immunomodulatory fibrous hyaluronic acid-Fmoc-diphenylalanine-based hydrogel induces bone regeneration. *J Clin Periodontol* **2023**, *50* (2), 200-219, https://doi.org/10.1111/jcpe.13725. DOI: 10.1111/jcpe.13725 (acccessed 2023/01/31). From NLM Medline.

(17) Nakkala, J. R.; Yao, Y.; Zhai, Z.; Duan, Y.; Zhang, D.; Mao, Z.; Lu, L.; Gao, C. Dimethyl Itaconate-Loaded Nanofibers Rewrite Macrophage Polarization, Reduce Inflammation, and Enhance Repair of Myocardic Infarction. *Small* **2021**, *17* (17), e2006992. DOI: 10.1002/smll.202006992 (acccessed 2023/12/11). From NLM Medline. Jia, Y.; Yang, W.; Zhang, K.; Qiu, S.; Xu, J.; Wang, C.; Chai, Y. Nanofiber arrangement regulates peripheral nerve regeneration through differential modulation of macrophage phenotypes. *Acta Biomater* **2019**, *83*, 291-301. DOI: 10.1016/j.actbio.2018.10.040 From NLM Medline. Ren, Y.; Chen, Y.; Chen, W.; Deng, H.; Li, P.; Liu, Y.; Gao, C.; Tian, G.; Ning, C.; Yuan, Z.; et al. Hydrophilic nanofibers with aligned topography modulate macrophage-mediated host responses via the NLRP3 inflammasome. *J Nanobiotechnology*

2023, *21* (1), 269. DOI: 10.1186/s12951-023-02024-9 From NLM Medline. Taskin, M. B.; Tylek, T.; Blum, C.; Bohm, C.; Wiesbeck, C.; Groll, J. Inducing Immunomodulatory Effects on Human Macrophages by Multifunctional NCO-sP(EO-stat-PO)/Gelatin Hydrogel Nanofibers. *ACS Biomater Sci Eng* **2021**, *7* (7), 3166-3178. DOI: 10.1021/acsbiomaterials.1c00232 From NLM Medline.

(18) Kumar, V. A.; Taylor, N. L.; Shi, S.; Wickremasinghe, N. C.; D'Souza, R. N.; Hartgerink, J. D. Self-assembling multidomain peptides tailor biological responses through biphasic release. *Biomaterials* **2015**, *52*, 71-78. DOI: https://doi.org/10.1016/j.biomaterials.2015.01.079.

(19) Whitesides, G. M.; Grzybowski, B. Self-assembly at all scales. *Science* **2002**, *295* (5564), 2418-2421. DOI: 10.1126/science.1070821.

(20) Edwards-Gayle, C. J. C.; Wychowaniec, J. K. Characterization of Peptide-Based Nanomaterials. In *Peptide Bionanomaterials*, Elsawy, M. A. Ed.; Springer International Publishing, 2023; pp 255-308.

(21) Zhang, K.; Zhang, H.; Gao, Y. H.; Wang, J. Q.; Li, Y.; Cao, H.; Hu, Y.; Wang, L. A Monotargeting Peptidic Network Antibody Inhibits More Receptors for Anti-Angiogenesis. *ACS Nano* **2021**, *15* (8), 13065-13076. DOI: 10.1021/acsnano.1c02194 From NLM Medline. Ligorio, C.; Mata, A. Synthetic extracellular matrices with function-encoding peptides. *Nat Rev Bioeng* **2023**, *1* (7), 1-19. DOI: 10.1038/s44222-023-00055-3 From NLM Publisher.

(22) Tang, Y.; Bera, S.; Yao, Y.; Zeng, J.; Lao, Z.; Dong, X.; Gazit, E.; Wei, G. Prediction and characterization of liquid-liquid phase separation of minimalistic peptides. *Cell Reports Physical Science* **2021**, 100579. DOI: https://doi.org/10.1016/j.xcrp.2021.100579.

(23) Pappas, C. G.; Shafi, R.; Sasselli, I. R.; Siccardi, H.; Wang, T.; Narang, V.; Abzalimov, R.; Wijerathne, N.; Ulijn, R. V. Dynamic peptide libraries for the discovery of supramolecular nanomaterials. *Nature Nanotechnology* **2016**, *11* (11), 960-967. DOI: 10.1038/nnano.2016.169.

(24) Saiani, A.; Mohammed, A.; Frielinghaus, H.; Collins, R.; Hodson, N.; Kielty, C. M.; Sherratt, M. J.; Miller, A. F. Self-assembly and gelation properties of alpha-helix versus beta-sheet forming

peptides. *Soft Matter* **2009**, *5* (1), 193-202. DOI: 10.1039/b811288f. Schneider, J. P.; Pochan, D. J.; Ozbas, B.; Rajagopal, K.; Pakstis, L.; Kretsinger, J. Responsive hydrogels from the intramolecular folding and self-assembly of a designed peptide. *Journal of the American Chemical Society* **2002**, *124* (50), 15030-15037. DOI: 10.1021/ja027993g. Mart, R. J.; Osborne, R. D.; Stevens, M. M.; Ulijn, R. V. Peptide-based stimuli-responsive biomaterials. *Soft Matter* **2006**, *2* (10), 822-835. DOI: 10.1039/b607706d. Wang, Y.; Geng, Q.; Zhang, Y.; Adler-Abramovich, L.; Fan, X.; Mei, D.; Gazit, E.; Tao, K. Fmoc-diphenylalanine gelating nanoarchitectonics: A simplistic peptide self-assembly to meet complex applications. *J Colloid Interface Sci* **2023**, *636*, 113-133. DOI: 10.1016/j.jcis.2022.12.166 From NLM Medline.

(25) Sheehan, F.; Sementa, D.; Jain, A.; Kumar, M.; Tayarani-Najjaran, M.; Kroiss, D.; Ulijn, R. V. Peptide-Based Supramolecular Systems Chemistry. *Chemical Reviews* **2021**. DOI: 10.1021/acs.chemrev.1c00089. Kralj, S.; Bellotto, O.; Parisi, E.; Garcia, A. M.; Iglesias, D.; Semeraro, S.; Deganutti, C.; D'Andrea, P.; Vargiu, A. V.; Geremia, S.; et al. Heterochirality and Halogenation Control Phe-Phe Hierarchical Assembly. *ACS Nano* **2020**, *14* (12), 16951-16961. DOI: 10.1021/acsnano.0c06041 From NLM PubMed-not-MEDLINE.

(26) Garcia, A. M.; Melchionna, M.; Bellotto, O.; Kralj, S.; Semeraro, S.; Parisi, E.; Iglesias, D.; D'Andrea, P.; De Zorzi, R.; Vargiu, A. V.; Marchesan, S. Nanoscale Assembly of Functional Peptides with Divergent Programming Elements. *ACS Nano* **2021**, *15* (2), 3015-3025. DOI: 10.1021/acsnano.0c09386 From NLM Medline.

(27) Wychowaniec, J. K.; Patel, R.; Leach, J.; Mathomes, R.; Chhabria, V.; Patil-Sen, Y.; Hidalgo-Bastida, A.; Forbes, R. T.; Hayes, J. M.; Elsawy, M. A. Aromatic Stacking Facilitated Self-Assembly of Ultrashort Ionic Complementary Peptide Sequence: beta-Sheet Nanofibers with Remarkable Gelation and Interfacial Properties. *Biomacromolecules* **2020**, *21* (7), 2670-2680. DOI: 10.1021/acs.biomac.0c00366 From NLM Medline.

(28) Wychowaniec, J. K.; Smith, A. M.; Ligorio, C.; Mykhaylyk, O. O.; Miller, A. F.; Saiani, A. Role of Sheet-Edge Interactions in β-sheet Self-Assembling Peptide Hydrogels. *Biomacromolecules* **2020**. DOI: 10.1021/acs.biomac.0c00229.

(29) Geckil, H.; Xu, F.; Zhang, X. H.; Moon, S.; Demirci, U. Engineering hydrogels as extracellular matrix mimics. *Nanomedicine* **2010**, *5* (3), 469-484. DOI: 10.2217/nnm.10.12.

(30) Nguyen, A. K.; Molley, T. G.; Kardia, E.; Ganda, S.; Chakraborty, S.; Wong, S. L.; Ruan, J.; Yee, B. E.; Mata, J.; Vijayan, A.; et al. Hierarchical assembly of tryptophan zipper peptides into stress-relaxing bioactive hydrogels. *Nat Commun* **2023**, *14* (1), 6604. DOI: 10.1038/s41467-023-41907-1 From NLM Medline.

(31) Farsheed, A. C.; Thomas, A. J.; Pogostin, B. H.; Hartgerink, J. D. 3D Printing of Self-Assembling Nanofibrous Multidomain Peptide Hydrogels. *Adv Mater* **2023**, *35* (11), e2210378. DOI: 10.1002/adma.202210378 (acccessed 2023/12/11). From NLM Medline.

(32) Treacy, N. J.; Clerkin, S.; Davis, J. L.; Kennedy, C.; Miller, A. F.; Saiani, A.; Wychowaniec, J. K.; Brougham, D. F.; Crean, J. Growth and differentiation of human induced pluripotent stem cell (hiPSC)-derived kidney organoids using fully synthetic peptide hydrogels. *Bioact Mater* **2023**, *21*, 142-156. DOI: 10.1016/j.bioactmat.2022.08.003 From NLM PubMed-not-MEDLINE.

(33) Lachowski, D.; Matellan, C.; Gopal, S.; Cortes, E.; Robinson, B. K.; Saiani, A.; Miller, A. F.; Stevens, M. M.; Del Rio Hernandez, A. E. Substrate Stiffness-Driven Membrane Tension Modulates Vesicular Trafficking via Caveolin-1. *ACS Nano* **2022**, *16* (3), 4322-4337. DOI: 10.1021/acsnano.1c10534 From NLM Medline.

(34) Zhang, S.; Marini, D. M.; Hwang, W.; Santoso, S. Design of nanostructured biological materials through self-assembly of peptides and proteins. *Current opinion in chemical biology* **2002**, *6* (6), 865-871. DOI: 10.1016/s1367-5931(02)00391-5 From NLM. Zhang, S.; Altman, M. Peptide self-assembly in functional polymer science and engineering. *Reactive and Functional Polymers* **1999**, *41* (1), 91-102. DOI: https://doi.org/10.1016/S1381-5148(99)00031-0.

(35) Wychowaniec, J. K.; Iliut, M.; Zhou, M.; Moffat, J.; Elsawy, M. A.; Pinheiro, W. A.; Hoyland, J. A.; Miller, A. F.; Vijayaraghavan, A.; Saiani, A. Designing Peptide/Graphene Hybrid Hydrogels through Fine-Tuning of Molecular Interactions. *Biomacromolecules* **2018**, *19* (7), 2731-2741. DOI: 10.1021/acs.biomac.8b00333 From NLM Medline.

(36) Aggeli, A.; Bell, M.; Carrick, L. M.; Fishwick, C. W. G.; Harding, R.; Mawer, P. J.; Radford, S. E.; Strong, A. E.; Boden, N. pH as a Trigger of Peptide β-Sheet Self-Assembly and Reversible Switching between Nematic and Isotropic Phases. *Journal of the American Chemical Society* **2003**, *125* (32), 9619-9628. DOI: 10.1021/ja021047i.

(37) Elsawy, M. A.; Smith, A. M.; Hodson, N.; Squires, A.; Miller, A. F.; Saiani, A. Modification of beta-Sheet Forming Peptide Hydrophobic Face: Effect on Self-Assembly and Gelation. *Langmuir* **2016**, *32* (19), 4917-4923. DOI: 10.1021/acs.langmuir.5b03841.

(38) Elsawy, M. A.; Wychowaniec, J. K.; Castillo Diaz, L. A.; Smith, A. M.; Miller, A. F.; Saiani, A. Controlling Doxorubicin Release from a Peptide Hydrogel through Fine-Tuning of Drug-Peptide Fiber Interactions. *Biomacromolecules* **2022**, *23* (6), 2624-2634. DOI: 10.1021/acs.biomac.2c00356 From NLM Medline.

(39) Rudra, J. S.; Tian, Y. F.; Jung, J. P.; Collier, J. H. A self-assembling peptide acting as an immune adjuvant. *Proceedings of the National Academy of Sciences* **2010**, *107* (2), 622-627. DOI: 10.1073/pnas.0912124107 (acccessed 2024/03/21). Si, Y.; Wen, Y.; Kelly, S. H.; Chong, A. S.; Collier, J. H. Intranasal delivery of adjuvant-free peptide nanofibers elicits resident CD8+ T cell responses. *Journal of Controlled Release* **2018**, *282*, 120-130. DOI: https://doi.org/10.1016/j.jconrel.2018.04.031. Votaw, N. L.; Collier, L.; Curvino, E. J.; Wu, Y.; Fries, C. N.; Ojeda, M. T.; Collier, J. H. Randomized peptide assemblies for enhancing immune responses to nanomaterials. *Biomaterials* **2021**, *273*, 120825. DOI: https://doi.org/10.1016/j.biomaterials.2021.120825. Mora-Solano, C.; Wen, Y.; Han, H.; Chen, J.; Chong, A. S.; Miller, M. L.; Pompano, R. R.; Collier, J. H. Active immunotherapy for TNF-mediated

inflammation using self-assembled peptide nanofibers. *Biomaterials* **2017**, *149*, 1-11. DOI: https://doi.org/10.1016/j.biomaterials.2017.09.031.

(40) Rudra, J. S.; Sun, T.; Bird, K. C.; Daniels, M. D.; Gasiorowski, J. Z.; Chong, A. S.; Collier, J. H. Modulating Adaptive Immune Responses to Peptide Self-Assemblies. *ACS Nano* **2012**, *6* (2), 1557-1564. DOI: 10.1021/nn204530r.

(41) Wen, Y.; Waltman, A.; Han, H.; Collier, J. H. Switching the Immunogenicity of Peptide Assemblies Using Surface Properties. *ACS Nano* **2016**, *10* (10), 9274-9286. DOI: 10.1021/acsnano.6b03409.

(42) Lee, J.; Ju, M.; Cho, O. H.; Kim, Y.; Nam, K. T. Tyrosine-Rich Peptides as a Platform for Assembly and Material Synthesis. *Adv Sci (Weinh)* **2019**, *6* (4), 1801255. DOI: 10.1002/advs.201801255 (acccessed 2023/12/11). From NLM PubMed-not-MEDLINE. Niazov-Elkan, A.; Weissman, H.; Shimoni, E.; Sui, X.; Feldman, Y.; Wagner, H. D.; Rybtchinski, B. Emergent Self-Assembly of Sustainable Plastics Based on Amino Acid Nanocrystals. *ACS Nano* **2023**, *17* (21), 20962-20967. DOI: 10.1021/acsnano.3c02528 From NLM PubMed-not-MEDLINE. Ji, W.; Xue, B.; Arnon, Z. A.; Yuan, H.; Bera, S.; Li, Q.; Zaguri, D.; Reynolds, N. P.; Li, H.; Chen, Y.; et al. Rigid Tightly Packed Amino Acid Crystals as Functional Supramolecular Materials. *ACS Nano* **2019**, *13* (12), 14477-14485. DOI: 10.1021/acsnano.9b08217 From NLM PubMed-not-MEDLINE.

(43) Ding, Y.; Li, Y.; Qin, M.; Cao, Y.; Wang, W. Photo-Cross-Linking Approach to Engineering Small Tyrosine-Containing Peptide Hydrogels with Enhanced Mechanical Stability. *Langmuir* **2013**, *29* (43), 13299-13306. DOI: 10.1021/la4029639.

(44) Wychowaniec, J. K.; Bektas, E. I.; Vernengo, A. J.; Mürner, M.; Airoldi, M.; Eglin, D.; D'Este, M. Effect of molecular weight of tyramine-modified hyaluronan on polarization state of peripheral blood mononuclear cells-derived macrophages. *bioRxiv* **2024**, 2024.2001. 2011.575241.

(45) Gao, J.; Tang, C.; Smith, A. M.; Miller, A. F.; Saiani, A. Controlling self-assembling peptide hydrogel properties through network topology. *Biomacromolecules* **2017**. DOI: 10.1021/acs.biomac.6b01693.

(46) Wychowaniec, J. K.; Moffat, J.; Saiani, A. Quantitative nanomechanical properties evaluation of a family of beta-sheet peptide fibres using rapid bimodal AFM. *J Mech Behav Biomed Mater* **2021**, *124*, 104776. DOI: 10.1016/j.jmbbm.2021.104776 From NLM Medline.

(47) Nelson, D. L.; Lehninger, A. L.; Cox, M. M. *Lehninger Principles of biochemistry*; Basingstoke, 2017.

(48) Pace, C. N.; Horn, G.; Hebert, E. J.; Bechert, J.; Shaw, K.; Urbanikova, L.; Scholtz, J. M.; Sevcik, J. Tyrosine hydrogen bonds make a large contribution to protein stability11Edited by C. R. Matthews. *Journal of Molecular Biology* **2001**, *312* (2), 393-404. DOI: https://doi.org/10.1006/jmbi.2001.4956. Balasco, N.; Altamura, D.; Scognamiglio, P. L.; Sibillano, T.; Giannini, C.; Morelli, G.; Vitagliano, L.; Accardo, A.; Diaferia, C. Self-Assembled Materials Based on Fully Aromatic Peptides: The Impact of Tryptophan, Tyrosine, and Dopa Residues. *Langmuir* **2024**, *40* (2), 1470-1486. DOI: 10.1021/acs.langmuir.3c03214 From NLM Medline.

(49) Adorinni, S.; Gentile, S.; Bellotto, O.; Kralj, S.; Parisi, E.; Cringoli, M. C.; Deganutti, C.; Malloci, G.; Piccirilli, F.; Pengo, P.; et al. Peptide Stereochemistry Effects from pK(a)-Shift to Gold Nanoparticle Templating in a Supramolecular Hydrogel. *ACS Nano* **2024**, *18* (4), 3011-3022. DOI: 10.1021/acsnano.3c08004 From NLM Medline.

(50) Grimsley, G. R.; Scholtz, J. M.; Pace, C. N. A summary of the measured pK values of the ionizable groups in folded proteins. *Protein Science* **2009**, *18* (1), 247-251, https://doi.org/10.1002/pro.19. DOI: https://doi.org/10.1002/pro.19 (acccessed 2021/03/03).

(51) Caplan, M. R.; Moore, P. N.; Zhang, S. G.; Kamm, R. D.; Lauffenburger, D. A. Self-assembly of a beta-sheet protein governed by relief of electrostatic repulsion relative to van der Waals attraction. *Biomacromolecules* **2000**, *1* (4), 627-631. DOI: 10.1021/bm005586w. Aggeli, A.; Bell,

M.; Boden, N.; Carrick, L. M.; Strong, A. E. Self-assembling peptide polyelectrolyte beta-sheet complexes form nematic hydrogels. *Angew. Chem., Int. Ed.* **2003**, *42* (45), 5603-5606.

(52) Tang, C.; Smith, A. M.; Collins, R. F.; Ulijn, R. V.; Saiani, A. Fmoc-Diphenylalanine Self-Assembly Mechanism Induces Apparent pK(a) Shifts. *Langmuir* **2009**, *25* (16), 9447-9453. DOI: 10.1021/la900653q.

(53) Hamley, I. W. Peptide fibrillization. *Angewandte Chemie-International Edition* **2007**, *46* (43), 8128-8147. DOI: 10.1002/anie.200700861. Xing, Z.; Chen, Y.; Qiu, F. Alternative Causal Link between Peptide Fibrillization and β-Strand Conformation. *ACS Omega* **2021**, *6* (19), 12904-12912. DOI: 10.1021/acsomega.1c01423.

(54) Boothroyd, S.; Miller, A. F.; Saiani, A. From fibres to networks using self-assembling peptides. *Faraday Discussions* **2013**, *166* (0), 195-207, 10.1039/C3FD00097D. DOI: 10.1039/C3FD00097D.

(55) Barth, A. Infrared spectroscopy of proteins. *Biochimica Et Biophysica Acta-Bioenergetics* **2007**, *1767* (9), 1073-1101. DOI: 10.1016/j.bbabio.2007.06.004.

(56) Barth, A.; Zscherp, C. What vibrations tell us about proteins. *Quarterly Reviews of Biophysics* **2002**, *35* (4), 369-430. DOI: 10.1017/s0033583502003815.

(57) Barth, A. The infrared absorption of amino acid side chains. *Progress in Biophysics & Molecular Biology* **2000**, *74* (3-5), 141-173. DOI: 10.1016/s0079-6107(00)00021-3.

(58) Guimarães, C. F.; Gasperini, L.; Marques, A. P.; Reis, R. L. The stiffness of living tissues and its implications for tissue engineering. *Nature Reviews Materials* **2020**, *5* (5), 351-370. DOI: 10.1038/s41578-019-0169-1.

(59) Chaudhuri, O.; Cooper-White, J.; Janmey, P. A.; Mooney, D. J.; Shenoy, V. B. Effects of extracellular matrix viscoelasticity on cellular behaviour. *Nature* **2020**, *584* (7822), 535-546. DOI: 10.1038/s41586-020-2612-2 From NLM Medline.

(60) Hamley, I. W. Form Factor of Helical Ribbons. *Macromolecules* **2008**, *41* (22), 8948-8950. DOI: 10.1021/ma8014917.

(61) Schwab, A.; Levato, R.; D'Este, M.; Piluso, S.; Eglin, D.; Malda, J. Printability and Shape Fidelity of Bioinks in 3D Bioprinting. *Chem Rev* **2020**, *120* (19), 11028-11055. DOI: 10.1021/acs.chemrev.0c00084 From NLM Medline.

(62) Singh, K.; Wychowaniec, J. K.; Edwards-Gayle, C. J. C.; Reynaud, E. G.; Rodriguez, B. J.; Brougham, D. F. Structure-dynamics correlations in composite PF127-PEG-based hydrogels; cohesive/hydrophobic interactions determine phase and rheology and identify the role of micelle concentration in controlling 3D extrusion printability. *J Colloid Interface Sci* **2024**, *660*, 302-313. DOI: 10.1016/j.jcis.2023.12.151 From NLM PubMed-not-MEDLINE.

(63) Chiesa, I.; Ligorio, C.; Bonatti, A. F.; De Acutis, A.; Smith, A. M.; Saiani, A.; Vozzi, G.; De Maria, C. Modeling the Three-Dimensional Bioprinting Process of beta-Sheet Self-Assembling Peptide Hydrogel Scaffolds. *Front Med Technol* **2020**, *2*, 571626, 10.3389/fmedt.2020.571626. DOI: 10.3389/fmedt.2020.571626 From NLM PubMed-not-MEDLINE.

(64) Liu, T.; Zhang, L.; Joo, D.; Sun, S.-C. NF-κB signaling in inflammation. *Signal Transduction and Targeted Therapy* **2017**, *2* (1), 17023. DOI: 10.1038/sigtrans.2017.23.

(65) Zhi, Y.; Lu, H.; Duan, Y.; Sun, W.; Guan, G.; Dong, Q.; Yang, C. Involvement of the nuclear factor-κB signaling pathway in the regulation of CXC chemokine receptor-4 expression in neuroblastoma cells induced by tumor necrosis factor-α. *Int J Mol Med* **2015**, *35* (2), 349-357. DOI: 10.3892/ijmm.2014.2032.

(66) Sapudom, J.; Mohamed, W. K. E.; Garcia-Sabate, A.; Alatoom, A.; Karaman, S.; Mahtani, N.; Teo, J. C. Collagen Fibril Density Modulates Macrophage Activation and Cellular Functions during Tissue Repair. *Bioengineering (Basel)* **2020**, *7* (2), 33. DOI: 10.3390/bioengineering7020033 From NLM PubMed-not-MEDLINE.

(67) Shapouri-Moghaddam, A.; Mohammadian, S.; Vazini, H.; Taghadosi, M.; Esmaeili, S. A.; Mardani, F.; Seifi, B.; Mohammadi, A.; Afshari, J. T.; Sahebkar, A. Macrophage plasticity,

polarization, and function in health and disease. *J Cell Physiol* **2018**, *233* (9), 6425-6440. DOI: 10.1002/jcp.26429 (acccessed 2024/01/29). From NLM Medline.

(68) Sapudom, J.; Karaman, S.; Mohamed, W. K. E.; Garcia-Sabaté, A.; Quartey, B. C.; Teo, J. C. M. 3D in vitro M2 macrophage model to mimic modulation of tissue repair. *npj Regenerative Medicine* **2021**, *6* (1), 83. DOI: 10.1038/s41536-021-00193-5.

(69) Sapudom, J.; Wu, X.; Chkolnikov, M.; Ansorge, M.; Anderegg, U.; Pompe, T. Fibroblast fate regulation by time dependent TGF-β1 and IL-10 stimulation in biomimetic 3D matrices. *Biomaterials Science* **2017**, *5* (9), 1858-1867, 10.1039/C7BM00286F. DOI: 10.1039/C7BM00286F.

(70) Wang, D.; Bratlie, K. M. Influence of Polymer Chemistry on Cytokine Secretion from Polarized Macrophages. *ACS Biomaterials Science & Engineering* **2015**, *1* (3), 166-174. DOI: 10.1021/ab5001063.

(71) Hedrich, C.; Bream, J. Cell type-specific regulation of IL-10 expression in inflammation and disease. *Immunologic research* **2010**, *47*, 185-206. DOI: 10.1007/s12026-009-8150-5. Kozicky, L. K.; Menzies, S. C.; Zhao, Z. Y.; Vira, T.; Harnden, K.; Safari, K.; Del Bel, K. L.; Turvey, S. E.; Sly, L. M. IVIg and LPS Co-stimulation Induces IL-10 Production by Human Monocytes, Which Is Compromised by an FcgammaRIIA Disease-Associated Gene Variant. *Front Immunol* **2018**, *9*, 2676, Original Research. DOI: 10.3389/fimmu.2018.02676 From NLM Medline.

(72) Haddy, N.; Sass, C.; Maumus, S.; Marie, B.; Droesch, S.; Siest, G.; Lambert, D.; Visvikis, S. Biological variations, genetic polymorphisms and familial resemblance of TNF-α and IL-6 concentrations: STANISLAS cohort. *European Journal of Human Genetics* **2005**, *13* (1), 109-117. DOI: 10.1038/sj.ejhg.5201294.

(73) Hou, J.; Yang, R.; Vuong, I.; Li, F.; Kong, J.; Mao, H. Q. Biomaterials strategies to balance inflammation and tenogenesis for tendon repair. *Acta Biomater* **2021**, *130*, 1-16. DOI: 10.1016/j.actbio.2021.05.043 From NLM Medline.

(74) Faroni, A.; Workman, V. L.; Saiani, A.; Reid, A. J. Self-Assembling Peptide Hydrogel Matrices Improve the Neurotrophic Potential of Human Adipose-Derived Stem Cells. *Adv Healthc Mater* **2019**, *8* (17), e1900410. DOI: 10.1002/adhm.201900410 (acccessed 2020/08/12). From NLM Medline.

(75) Sceglovs, A.; Wychowaniec, J. K.; Skadins, I.; Reinis, A.; Edwards-Gayle, C. J. C.; D'Este, M.; Salma-Ancane, K. Effect of steam sterilisation on physico-chemical properties of antibacterial covalently cross-linked ε-polylysine/hyaluronic acid hydrogels. *Carbohydrate Polymer Technologies and Applications* **2023**, *6*, 100363. DOI: 10.1016/j.carpta.2023.100363. Cowieson, N. P.; Edwards-Gayle, C. J. C.; Inoue, K.; Khunti, N. S.; Doutch, J.; Williams, E.; Daniels, S.; Preece, G.; Krumpa, N. A.; Sutter, J. P.; et al. Beamline B21: high-throughput small-angle X-ray scattering at Diamond Light Source. *J Synchrotron Radiat* **2020**, *27* (Pt 5), 1438-1446. DOI: 10.1107/S1600577520009960 From NLM PubMed-not-MEDLINE. Edwards-Gayle, C. J. C.; Khunti, N.; Hamley, I. W.; Inoue, K.; Cowieson, N.; Rambo, R. Design of a multipurpose sample cell holder for the Diamond Light Source high-throughput SAXS beamline B21. *J Synchrotron Radiat* **2021**, *28* (Pt 1), 318-321. DOI: 10.1107/S1600577520013831 From NLM PubMed-not-MEDLINE.

(76) Hinton, T. J.; Hudson, A.; Pusch, K.; Lee, A.; Feinberg, A. W. 3D Printing PDMS Elastomer in a Hydrophilic Support Bath via Freeform Reversible Embedding. *ACS Biomaterials Science & Engineering* **2016**, *2* (10), 1781-1786. DOI: 10.1021/acsbiomaterials.6b00170.

(77) Razzi, F.; Fratila-Apachitei, L. E.; Fahy, N.; Bastiaansen-Jenniskens, Y. M.; Apachitei, I.; Farrell, E.; Zadpoor, A. A. Immunomodulation of surface biofunctionalized 3D printed porous titanium implants. *Biomed Mater* **2020**, *15* (3), 035017. DOI: 10.1088/1748-605X/ab7763. Utomo, L.; Boersema, G. S. A.; Bayon, Y.; Lange, J. F.; van Osch, G.; Bastiaansen-Jenniskens, Y. M. In vitro modulation of the behavior of adhering macrophages by medications is biomaterial-dependent. *Biomed Mater* **2017**, *12* (2), 025006. DOI: 10.1088/1748-605X/aa5cbc.